

Deuterium abundance toward G191-B2B: Results from the Far Ultraviolet Spectroscopic Explorer (*FUSE*) Mission ¹

M. Lemoine, A. Vidal-Madjar, G. Hébrard, J.-M. Désert, R. Ferlet, A. Lecavelier des Etangs

Institut d'Astrophysique de Paris, CNRS, 98 bis bld Arago, F-75014 Paris, France

J.C. Howk, M. André, W.P. Blair, S.D. Friedman, J.W. Kruk, S. Lacour, H.W. Moos, K. Sembach,

Department of Physics and Astronomy, Johns Hopkins University, Baltimore, MD 21218, USA

P. Chayer

UVIC/Department of Physics and Astronomy, Department of Physics and Astronomy, Johns Hopkins University, Baltimore, MD 21218, USA

E.B. Jenkins

Princeton University Observatory, Princeton, NJ 08544, USA

D. Koester

Institut für Theoretische Physik und Astrophysik, Universität Kiel, D-24098 Kiel, Germany

J.L. Linsky, B.E. Wood

JILA, University of Colorado and NIST, Boulder, CO 80309-0440, USA

W.R. Oegerle, G. Sonneborn

Laboratory for Astronomy and Solar Physics, NASA/GSFC, Code 681, Greenbelt, MD 20771, USA

and

D.G. York

Dept. of Astronomy & Astrophysics, University of Chicago, Chicago, IL 60637, USA

ABSTRACT

High-resolution spectra of the hot white dwarf G191-B2B, covering the wavelength region 905–1187Å, were obtained with the Far Ultraviolet Spectroscopic Explorer (*FUSE*). This data was used in conjunction with existing high-resolution Hubble Space Telescope STIS observations to evaluate the total H I, D I, O I and N I column densities along the line of sight. Previous determinations of $N(\text{D I})$ based upon GHRS and STIS observations were controversial due to the saturated strength of the D I Lyman α line. In the present analysis the column density of D I has been measured using only the unsaturated Lyman β and Lyman γ lines observed by *FUSE*. A careful inspection of possible systematic uncertainties tied to the modeling of the stellar continuum or to the uncertainties in the *FUSE* instrumental characteristics has been performed. The column densities derived are: $\log N(\text{D I}) = 13.40 \pm 0.07$, $\log N(\text{O I}) = 14.86 \pm 0.07$, and $\log N(\text{N I}) = 13.87 \pm 0.07$ quoted with 2σ uncertainties.

The measurement of the H I column density by profile fitting of the Lyman α line has been found to be unsecure. If additional weak hot interstellar components are added to the three detected clouds along the line of sight, the H I column density can be reduced quite significantly, even though the signal-to-noise ratio and spectral resolution at Lyman α are excellent. The new estimate of $N(\text{H I})$ toward G191-B2B reads: $\log N(\text{H I}) = 18.18 \pm 0.18$ (2σ uncertainty), so that the average (D/H) ratio on the line of sight is: $(\text{D}/\text{H}) = 1.66^{+0.9}_{-0.6} \times 10^{-5}$ (2σ uncertainty).

Subject headings: ISM: abundances : ISM — ultraviolet

1. Introduction

Deuterium is thought to be produced in significant amount only during primordial Big Bang nucleosynthesis (BBN), and to be thoroughly destroyed in stellar interiors. Deuterium is thus a key element in cosmology and in Galactic chemical evolution (see e.g. Audouze & Tinsley 1976; Gautier & Owen 1983; Vidal-Madjar & Gry 1984; Boesgaard & Steigman 1985; Olive *et al.* 1990; Pagel 1992; Vangioni-Flam & Cassé 1994; Vangioni-Flam *et al.* 1995; Prantzos 1996; Scully *et al.* 1997; Cassé & Vangioni-Flam 1998; Tosi *et al.* 1998). Indeed, its primordial abundance is the best tracer of the baryonic density parameter of the

¹This work is based on data obtained for the Guaranteed Time Team by the NASA-CNES-CSA *FUSE* mission operated by the Johns Hopkins University.

Universe, Ω_B , and the decrease in its abundance during galactic evolution traces the cosmic star formation rate at various epochs.

The first (indirect) measurement of the deuterium abundance was carried out using ^3He in the solar wind, giving the presolar value $\text{D}/\text{H} \simeq 2.5 \pm 1.0 \times 10^{-5}$ (Geiss & Reeves 1972). The first measurements of the D/H ratio in the interstellar medium (ISM) were reported shortly thereafter by Rogerson & York (1973), and their value $(\text{D}/\text{H}) \simeq 1.4 \pm 0.2 \times 10^{-5}$ has remained a landmark average value for the interstellar D/H ratio. Finally direct measurements of the primordial (D/H) ratio in low-metallicity material at high redshift have been successfully carried out these past few years (e.g., Burles 2001 for a review, and references therein). The values derived cluster around $(\text{D}/\text{H}) \sim 3 \times 10^{-5}$ although with significant dispersion, which may or may not be real. Quite similarly the measurements of the (D/H) ratio in the Galactic ISM towards hot stars with the *Copernicus* satellite lead to many evaluations of D/H (see e.g. York and Rogerson 1976; Vidal-Madjar *et al.* 1977; Laurent *et al.* 1979; Ferlet *et al.* 1980; York 1983; Allen *et al.* 1992) which also show dispersion around the above York & Rogerson (1973) value. This dispersion has been recently confirmed by IMAPS observations (Jenkins *et al.* 1999; Sonneborn *et al.* 2000), indicating that the D/H ratio may vary by a factor $\simeq 3$ in the solar neighborhood, i.e., within a few hundred parsecs.

In this paper we present a new determination of the D/H ratio on the line of sight to the nearby DA white dwarf (WD) G191-B2B based on observations obtained with the Far Ultraviolet Spectroscopic Explorer (*FUSE*, Moos *et al.* 2000; Sahnou *et al.* 2000). This paper is one of a series in this volume describing the first results of the *FUSE* (D/H) program in the Local ISM (LISM). This program and its results are summarized in the overview paper by Moos *et al.* (2002).

Observing white dwarfs has many advantages over hot and cool stars for studying the D/H ratio, as explained in Vidal-Madjar *et al.* (1998): these targets can be chosen close to the Sun, in order to avoid a complex line of sight structure, and in the high temperature range, so that the interstellar absorption is superimposed on a smooth stellar continuum. The risk of contamination by low column density H I fluffs possibly present in the hot star winds (Gry, Lamers & Vidal-Madjar 1984) is negligible for WDs, and their hot continuum offers the possibility of observing the numerous UV lines of N I and especially O I, which is a very useful tracer of H I and D I. The (D/H) ratio has already been measured toward four white dwarfs, using the HST: G191-B2B (Lemoine *et al.* 1996; Vidal-Madjar *et al.* 1998; Sahu *et al.* 1999), HZ43A (Landsman *et al.* 1996), Sirius B (Hébrard *et al.* 1999) and Feige 24 (Vennes *et al.* 2000). For HZ43A, Sirius B and Feige 24 the average D/H values obtained are compatible with the local ISM (LISM) D/H determination (Linsky 1998) made within the Local Interstellar Cloud (the LIC in which the sun is embedded), although in the

case of Sirius B this compatibility is marginal.

In the case of G191-B2B, it was found that the line of sight comprises one neutral region corresponding to the LIC, and two more ionized absorbing components (Lemoine *et al.* 1996; Vidal-Madjar *et al.* 1998). The average (D/H) ratio (defined as the ratio of the total column densities of D I and H I) was found to be $(D/H) = 1.12 \pm 0.08 \times 10^{-5}$ (Vidal-Madjar *et al.* 1998), significantly different from the value measured toward Capella $(D/H)_{LIC} = 1.5 \pm 0.1 \times 10^{-5}$ (Linsky 1998). The (D/H) ratio measured toward G191-B2B has been contested by Sahu *et al.* (1999), who used STIS data and concluded to the presence of two interstellar components only, and to a D/H ratio compatible with that observed toward Capella. The disagreement resides in the evaluation of the total D I column density (Vidal-Madjar 2000; Sahu 2000), and arises presumably because the Lyman α D line is saturated and the column density is thus sensitive to the line profile. The number of components assumed on the line of sight may also introduce differences between the analyses of these groups (see Vidal-Madjar 2001 for a detailed discussion).

In the present work we re-examine these issues, making use of high quality *FUSE* and STIS observations of G191-B2B. We first measure the $N(D\text{ I})$, $N(O\text{ I})$ and $N(N\text{ I})$ column densities using the unsaturated lines of these elements in the *FUSE* datasets, notably Lyman β and Lyman γ for D I (Section 2). We then analyze the recent high quality STIS observations in Section 3, and provide explicit evidence for the presence of three absorbing components (at least) on the line of sight. We also provide a refined estimate of the total H I column density. All throughout this work, considerable effort has been put on quantifying possible systematic uncertainties related to fixed-pattern noise, detector artifacts, background uncertainties, wavelength calibration and modeling of the stellar continua, as well as to the velocity structure of the line of sight. In particular, we argue in Section 3.3 that previous estimates of the total $N(H\text{ I})$ are subject to a large systematic uncertainty related to the possible presence of additional weak $[N(H\text{ I}) \leq 10^{14} \text{ cm}^{-2}]$ hot ($T \sim 10^5 \text{ K}$) components. This effect may have a large impact on our understanding of the observed variations of the (D/H) ratio in the ISM, as it may affect other lines of sight, and is the subject of a companion paper (Vidal-Madjar & Ferlet 2002). We provide a summary of our results and a short discussion in Section 4; an overall discussion of the *FUSE* results is given by Moos *et al.* (2002).

2. Column densities of D I, O I and N I measured with *FUSE*

The *FUSE* instrument (Moos *et al.* 2000; Sahnou *et al.* 2000) gives access to the wavelength range 905–1187Å on eight detector segments, through three different entrance

apertures (the large, medium and narrow apertures – LWRS, MDRS and HIRS, respectively) and four channels (two LiF and two SiC). In particular, it gives access to the higher order unsaturated Lyman lines of D I and can thus offer a reliable estimate of $N(\text{D I})$. Similarly, many weak lines of O I and N I are present in this bandpass, as shown in Table 1. The FUSE spectrum of G191-B2B in the SiC1B channel observed with the HIRS aperture is shown in Fig. 1, in which the lines of D I, N I, O I used in our study are indicated.

The white dwarf G191-B2B has been observed several times with *FUSE* through the three different entrance apertures; the observation log is given in Table 2. Since the target is point-like, the resolutions obtained with these apertures should not be too different, but there is a clear variation due to some off-axis effect when moving from one aperture to another. The main problem comes from the geocoronal Lyman β emission whose strength increases with the surface area of the aperture, and which blends with the interstellar H I absorption. This leads us to employ different approaches in the analysis of the data, depending upon the slit used, as discussed below.

The observations were treated through the version 1.8.7 of the CALFUSE pipeline. The data were then collected channel by channel by series of subexposures. Due to the sensitivity of *FUSE* and the brightness of the source, the data were obtained in the HISTOGRAM mode (a spectral imaging mode, in which a two-dimensional spectrum was accumulated onboard). Each subexposure has a S/N ratio that is high enough to clearly see the strong interstellar or photospheric features. The different subexposures could then be easily aligned on top of each other to compensate for the slow thermal drifts that displace the wavelength scale from one subexposure to another. These drifts never translates into more than ± 5 pixels. A high S/N spectrum is thus reconstructed in each channel and for each aperture. This process preserves the ultimate *FUSE* resolution and it also partly eliminates some of the detector’s fixed pattern noise by acting like a random FP-SPLIT procedure.

Since the *FUSE* sampling is ~ 10 pixels per resolution element, we rebinned the spectra by three. We measure column densities by profile fitting of the various lines observed, using the code `Owens.f` developed by one of us (M. L.) and the French *FUSE* team. Our general procedure for data analysis is as follows. We split each spectrum into a series of small sub-spectra centered on absorption lines to be analyzed, whose width is a few Å depending on the line density and fit all lines contained in all sub-spectra simultaneously. Between different sub-spectra, the zero-point velocity offset is left to vary to compensate for the wavelength calibration ripple effects in *FUSE* data; the Line Spread Function is generally taken to be a Gaussian whose FWHM varies freely during the fitting procedure and independently from sub-spectrum to sub-spectrum. It is also checked that considering a double Gaussian LSF with free widths, free amplitude ratio and zero pixel offset between the two Gaussian

components, does not change the results. The background levels used for each line are those evaluated at the bottom of the closest Lyman line (see Fig. 2 for an example), which leads to an upper limit for the derived column densities; fixing the background level at the 0 value gives access to the lower limit of the evaluated column densities. This uncertainty is taken into account in our procedure; however *FUSE* is operating in first order grating mounts and consequently the stray light level is generally quite low, as can be seen in Fig. 2 for Lyman γ . This analysis procedure allows to reduce systematic uncertainties tied to fixed pattern noise effects or detector artifacts and uncertain calibration, since different lines of the same elements observed through different apertures and in different channels are fitted simultaneously. For instance, if a given line is subject to an artifact in the dataset, the χ^2 of the fit in the region around this line, or equivalently the quality of the fit of this particular line should stand out in the overall fit if the number of lines analyzed is sufficiently large, as is the case here. Moreover, by letting the unknown instrumental parameters vary freely, i.e., the LSF shape and width, the background flux, the wavelength zero-point and the shape of the continuum, and be optimized simultaneously with the physical parameters that define the absorbers, one marginalizes the final result over these unknowns. Therefore the errors attached to the uncertainty on these above characteristics are included in the final errors quoted for the column densities. Finally, all lines are also analyzed one by one, i.e. each independently of all others, in order to check for overall consistency. A detailed discussion of this procedure and survey of possible systematic errors tied to *FUSE* data is given in a companion paper by Hébrard *et al.* (2002).

2.1. O I and N I

Since *FUSE* cannot resolve the velocity structure of the line of sight (see Section 3), we have used only unsaturated lines of D I, N I and O I and assumed only one interstellar component to be present. Therefore, all measured column densities in this Section are integrated over the line of sight. It has been verified that using three interstellar components in the fit of the *FUSE* did not change the conclusions as long as only non-saturated lines were considered; an example of single *vs* multiple component fits is shown in Fig. 2.

Note that HST observations cannot give a reliable measurement of the O I column density without a complete knowledge of the velocity and broadening structure of the line of sight since the only absorption line available at 1302Å is strongly saturated. In contrast the N I triplet at 1200Å in the GHRS or STIS bandpass is only moderately saturated and may provide a precise estimate of the total $N(\text{N I})$. The various measurements of $N(\text{N I})$ and $N(\text{O I})$ are listed in Table 3.

Since the contamination of interstellar lines by weak photospheric lines is a likely possibility in the *FUSE* spectral range due to the high density of atomic lines in this bandpass, we excluded from the fit all lines that presented an obviously excessive equivalent width or column density relative to the others. As an example as shown on Figure 3 the N I line at 954.1042Å is very probably blended with a photospheric line which shows up at nearly the same wavelength in the NLTE spectrum calculated with the TLUSTY/SYNSPEC codes (described in Section 3). Such blending becomes particularly important in the case of G191-B2B because the total O I or N I column densities are small, and their absorptions are relatively weak features which may be more easily blended with undetected photospheric ones. This is much less important for the other *FUSE* (D/H) targets (see the synthesis of *FUSE* results by Moos *et al.* 2002, and the individual line of sights studies by Friedman *et al.* 2002, Hébrard *et al.* 2002, Lehner *et al.* 2002, Sonneborn *et al.* 2002 and Wood *et al.* 2002) which present larger column densities, except for the white dwarf HZ43A (Kruk *et al.* 2002) which presents a pure H atmosphere (Barstow, Holberg & Koester 1995; Dupuis *et al.* 1998) and thus no possible blend with photospheric lines. However note that this line selection process may induce in the case of G191-B2B a slight underestimation of the total O I or N I column densities.

The O I and N I lines used in this study are listed in Table 1. Some of them were rejected either because they are saturated (marked “strong” in Table 1), or because of a blend with a photospheric feature (marked “blend”), or because they are too weak and subject to systematic effects of the noise (marked “weak”). Some were kept in one channel but not in an other if a nearby detector defect was identified. For this reason, having the same spectrum observed in different independent channels was extremely helpful.

By following the general method depicted above, the final column density determinations are :

$$\begin{aligned}\log N(\text{O I})_{\text{tot}} &= 14.86 (\pm 0.05) (\pm 0.04) \\ \log N(\text{N I})_{\text{tot}} &= 13.87 (\pm 0.05) (\pm 0.05)\end{aligned}$$

where the errors are first statistical (2σ) and second systematic (95.5% c.l.). The statistical errors were evaluated through the $\Delta\chi^2$ technique, an example of which is given for the $N(\text{D I})$ determination to follow. However, one important comment is of order at this point. The total χ^2 for all spectral lines fitted simultaneously (H I, D I, O I and N I) in the case of the HIRS observations is equal to 3211.44 for 1843 degrees of freedom (d.o.f.), even though the fit appears very satisfactory by eye. This χ^2 value lies well above the upper 95.5% confidence level limit for statistical fluctuation at 1966.71. We interpret this large χ^2 value as a result of a systematic underestimate of the magnitude of the individual pixel errors by the

instrument. In order to quantify this uncertainty, we have completed low order polynomial fits over relatively smooth and flat continuum sections close to each of the spectral lines analyzed. These simple fits gave a χ^2 of 688 for 500 degrees of freedom, again above the 95.5% c.l. upper limit at 563.9. This indicates that indeed the individual pixel errors are underestimated by instrument, probably due to the presence of fixed pattern noise in the data. The discrepancy in terms of ratio of measured to expected χ^2 is not as strong as for the best-fit χ^2 values, but this may be due to differences in the error levels for pixels located on the continuum and those located at the bottom of the saturated Lyman lines.

In order to compensate for these effects, we have thus decided to rescale all χ^2 measured, which amounts to an overall rescaling of the individual pixel error estimates. In particular, we have chosen to divide all χ^2 by $1.84 = 3211.44/1741.64$, where 1741.64 corresponds to the lowest expected χ^2 at the 95.5% confidence level for 1843 d.o.f. This rescaling rescales (increases) the error bars on the physical parameters that we derive since the $\Delta\chi^2$ contour levels are also rescaled. In effect, in order to derive the 3σ error bar around a single parameter minimum value, we search the values of this parameter that lead to an increase in (non-rescaled) χ^2 of $9 \times 1.84 = 16.6$ instead of 9. Our choice of rescaling is thus very conservative with respect to the final error bars measured. All presented FUSE statistical errors will be evaluated following this method.

The systematic errors quoted above for O I and N I reflect the range of values obtained for the best-fit solutions for different apertures, given in Table 3. Note that in this table, the errors quoted include the statistical error plus part of the above systematic errors, since it accounts for the differences measured between different observations, different channels and different spectral ranges where lines of the species concerned are seen, but observed through the same aperture (see the discussion in Hébrard *et al.* 2002). Note that the total O I or N I column density evaluations made with the LWRS+MDRS are in both cases lower than those made with the other apertures. We do not know the cause of this apparent systematic effect, but included it in the overall uncertainty on our result.

The quadratic sum of statistical and systematic uncertainties then leads to:

$$\begin{aligned}\log N(\text{O I})_{\text{tot}} &= 14.86 (\pm 0.07) \\ \log N(\text{N I})_{\text{tot}} &= 13.87 (\pm 0.07)\end{aligned}$$

2.2. Measurement of $N(\text{D I})$

In the *FUSE* bandpass, D I is clearly detected at Lyman β , weakly at Lyman γ , and not at Lyman δ . We list in Table 4 the different estimates of the total column density of D I

that have been obtained from HST observations of Lyman α , and which we measure using the present *FUSE* data. Here as well, we assumed that only one component is present on the line of sight since the D I lines are optically thin. Again we checked the impact of a more complex line of sight structure and found it to be negligible, as expected. We carried out the same investigations of systematic effects as for O I and N I, using the approach detailed above and in Hébrard *et al.* (2002).

There is however one essential difference between D I and O I or N I in terms of systematics. Namely the continuum to the D I absorption is provided by the blue wing of the corresponding H I absorption, while the continuum around the O I and N I is very smooth. It is thus necessary to measure the possible systematic tied to the estimate of the stellar continuum on the measurement of $N(\text{D I})$. In order to do so, we have measured $N(\text{D I})$ with and without beforehand correction of the data by a theoretical NLTE stellar continuum (described in Section 3). Some corresponding fits are shown in Fig. 2, and the best-fit to the HIRS data is shown in Fig. 4. The effect of any assumption on the stellar continuum was found to be negligible as compared to the statistical uncertainty.

However, we have found that the value of $N(\text{D I})$ measured if the H I lines are excluded from the fit and their blue wing modeled by a polynomial is higher than when the H I are included in the fit. This systematic effect may result from the following: in the latter (standard) approach, where both D I and H I are fitted together, the position of the D I absorption is tied to that of H I, i.e., they have the same radial velocity and their zero point wavelength offsets are the same as both lines appear in the same sub-spectrum. However, in the former approach, the velocity of D I is not subject to this constraint. These two approaches are denoted in Table 4 as “D I & H I” (standard approach) and “D I, no H I” for the other one. One should note that a discrepancy in radial velocity between the D I line and its counterpart H I could be attributed to small scale ripples in the *FUSE* wavelength calibration or to the presence of weak H I absorbers which would shift the position of the H I line with respect to that of the D I line in which these absorbers would not be felt. In this respect the approach in which D I is fitted independently of H I seems more adequate; however the interpolation of the blue wing of the H I line by a polynomial is not always straightforward. We should mention that this systematic effect is not fully understood and does not seem to be always present on different lines of sight. In any case it is included in our estimate of the systematic error.

Finally a small additional systematic effect is found to be attached to the uncertainty in the shape of the LSF, i.e. whether it is a single gaussian or a double gaussian with wide wings (indicated as “double LSF” in Table 4). As mentioned previously, a single gaussian LSF has a free FWHM in the fit, while a double gaussian LSF has free amplitude ratio

between both components, free FWHM for each, but separation between both components fixed to zero pixel. The impact of the shape of the LSF on the measured $N(\text{D I})$ is shown in Figure 5 where the $\Delta\chi^2$ is plotted as a function of $\log N(\text{D I})$. In practice this curve is calculated by fixing $\log N(\text{D I})$ to a given value, finding the best fit χ^2 for this value with all other parameters free, and plotting the difference between this χ^2 and the best χ^2 obtained for all possible values of $\log N(\text{D I})$. In this figure, the curvature of a $\Delta\chi^2$ curve gives the statistical error, as usual, while the relative shift between two curves corresponding to two different sets of assumptions is interpreted as an estimate of the 1σ systematic error tied to the uncertainty on the assumptions.

We thus conclude that the total D I column density on this line of sight measured using the HIRS data is:

$$\log N(\text{D I})_{\text{tot}}^{\text{HIRS}} = 13.39 \pm 0.07 \pm 0.06$$

where the errors are first statistical (2σ) and second systematics (95.5% c.l.).

Combining these errors leads to:

$$\log N(\text{D I})_{\text{tot}}^{\text{HIRS}} = 13.39 \pm 0.09$$

As can be seen from the comparison between the evaluations of $N(\text{D I})$ made for the different apertures, there is no significant systematic effect tied to the aperture, contrary to the analysis for O I and N I. The average $N(\text{D I})$ measured through the different apertures then reads:

$$\log N(\text{D I})_{\text{tot}} = 13.40 \pm 0.07$$

This value agrees with all previously measured values of $N(\text{D I})$ shown in Table 4, except with that of Sahu *et al.* (1999), using the STIS-Ech#1 data, which gave $\log N(\text{D I}) = 13.55^{+0.07}_{-0.08}$. It thus appears that the discrepancy between this value and the others should be attributed to the dataset used, in agreement with the conclusion of Vidal-Madjar (2001), and the debate around the value of $N(\text{D I})$ is now settled.

3. The velocity structure of the line of sight and $N(\text{H I})$

In this Section we analyze new high resolution high signal-to-noise STIS data of G191-B2B in order to determine the number of components on the line of sight and provide a new

estimate of the total neutral hydrogen column density. As mentioned in Section 1, there exists a controversy in the literature about the total number of absorbing components, as Sahu *et al.* (1999) claimed to see two only, whereas Vidal-Madjar *et al.* (1998) claimed that three at least were present. In this Section, we present concrete evidence in favor of the latter. Previous measurements of $N(\text{H I})$ are compiled in Table 5; these values scatter around a (non-weighted) mean $\log N(\text{H I}) = 18.34 \pm 0.03$ (the dispersion corresponds to the non-weighted dispersion of the individual measurements around the mean). Individual measurements tend not to agree with each other, and therefore a new independent estimate is useful. Moreover we argue in this Section that the total $N(\text{H I})$ toward G191-B2B is, as a matter of fact, much less well known than previously thought, since additional weak hot absorbing components may strongly affect the column density estimate from Lyman α . The new STIS data analyzed here represent about three times the total exposure time cumulated hitherto toward G191-B2B.

All STIS observations were extracted following the method of Howk and Sembach (2000). We selected spectral lines corresponding to N I, O I, Si II, Si III, C II, S II, S III in the E140H echelle configuration and Fe II lines in the E230H one, both at $R \simeq 90,000$ resolving power, as reported in Table 6. All these species are seen in one or more spectral lines, strong and/or weak, and cover a wide range of atomic masses, so that this data should provide strong constraints on the structure of the line of sight as well as on the component to component physical state and thermal and non-thermal broadening of each.

In order to verify that no photospheric line is blended with one of the interstellar lines analyzed, we have computed a synthetic spectrum of G191-B2B which includes all species observed in the atmosphere of G191-B2B, i.e., C, N, O, Si, P, S, Fe, and Ni (Lanz *et al.* 1996; Vennes *et al.* 1996). We employ the program TLUSTY developed by Hubeny & Lanz (1995) to compute a NLTE metal line-blanketed model by using the atmospheric parameters of Barstow *et al.* (1998), i.e., $\log g = 7.4$ and $T_{\text{eff}} = 54\,000\text{K}$, and the abundances determined by Barstow *et al.* (2001). From the comparison of the observations with the model calculation it was possible to select the lines where no or very weak photospheric features are coincident with the interstellar ones, as for the *FUSE* data. Furthermore it is possible that some photospheric lines are present but not predicted by the model; we thus fitted simultaneously as many different spectral lines of each species as available, in order to identify and minimize the effect of unpredicted photospheric lines, as was done for the analysis of the *FUSE* data. This approach also reduces the possible impact of instrumental defects which may be present in some area of the detector but not in others.

Following the general method of analysis described in the previous Section, we split the STIS data into sub-spectra, each of them centered on one spectral line and having typical

width $\sim 0.3\text{\AA}$. All sub-spectra are then fitted simultaneously. The wavelength zero point offsets are left free to vary during the fit. Note that shifts in the wavelength calibration from region to region could still be present even after a careful wavelength scale calibration. As an example, we detected an erroneous 4km s^{-1} wavelength shift between the GHRS Si III line position and that in the STIS data. After comparison with GHRS first order grating observations, we confirmed that the STIS calibration was correct, and the GHRS calibration erroneous. We found that the average relative shift between two spectral regions in the STIS data is $\simeq -0.1 \pm 1.1\text{km s}^{-1}$ (2σ error). An *rms* error of 0.5km s^{-1} in the STIS calibration is indeed compatible with the $\simeq 3.3\text{km s}^{-1}$ resolution of the instrument. The stellar continua in each region are interpolated by low order polynomials (except for Lyman α where the theoretical continuum is used in some cases, see below), and the background level in each region is determined using the closest saturated line. The typical background flux is $-2.6 \pm 2.4\%$ (2σ error) of the continuum for the E140H data, and $-0.10 \pm 4.2\%$ (2σ error) for the E230H data. Finally in some cases (see below for details), the LSF is left free to vary and corresponds either to a simple gaussian or to a double gaussian. Again, we emphasize that the uncertainty on these instrumental characteristics is contained in the final error bars given below, which we determine using a $\Delta\chi^2$ method, since the corresponding parameters are left free to vary during the fit.

In the case of the STIS observations made with the E140H and E230H echelle modes, we used the tabulated LSF, corresponding to the slit used for these observations (0.2×0.2 arc sec). This is an important issue because these LSFs possess wings that could have some impact on the precise determination of the physical parameters we are aiming at. To test the quality of the fits we also tried a single gaussian LSF with free FWHM. We found excellent fits with this freely variable width single gaussian LSF for both echelle datasets. We find for the E140H an average FWHM = $2.91(\pm 0.44)$ pixel (2σ) and for E230H, FWHM = $2.38(\pm 0.47)$ pixel (2σ). These determinations are certainly compatible with the tabulated LSF in terms of “average” widths, but are different in terms of shape. They correspond to 80,000 and 100,000 resolving power respectively for the E140H and E230H spectra. Finally, we also tested double gaussian LSFs but found no significant improvement. We thus decided to present results with both types of LSFs (free gaussians and tabulated) in order to show the stability and robustness of our column density determinations. As we will see, such a change has negligible impact on the derived total H I column density.

Following the analysis of the *FUSE* data, we evaluate the accuracy of the instrument estimate of the individual pixel errors by completing low order polynomial fits over relatively smooth and flat continuum sections close to each of the fitted spectral lines. These simple fits give a total $\chi^2 = 921.37$ (sum of all χ^2 in the different portions of continuum analyzed) for 661 degrees of freedom, which lies well above the upper 95.5% confidence level limit of

723.9 for a χ^2 distribution with 661 d.o.f. Therefore we rescale all χ^2 by a common factor $921.37/600.63 = 1.53$, where 600.63 corresponds to the lower 95.5% confidence level limit for 661 d.o.f.

Finally, in the course of the analysis, the physical characteristics of each absorbing component (velocity v , temperature T and micro-turbulent broadening ξ) are determined; however we will not provide a detailed analysis of these characteristics and their uncertainties since we are primarily interested in the total number of absorbing components and the total neutral hydrogen column density.

3.1. Number of absorbing components

In order to settle the debate on the total number of absorbing components, we have studied two and three component solutions. Simple eye inspection of the data indicates that at least two components are present on the line of sight; as mentioned previously, the red component can be identified with the LIC, a moderately neutral region, while the blue component is clearly more ionized, and, as we argue, more complex than a single absorber (see Vidal-Madjar *et al.* 1998 and Sahu *et al.* 1999).

The result of this analysis is summarized in Table 7, which gives the χ^2 values obtained for the fits of various spectral regions, and for all regions (excluding Lyman α), for two and three component solutions, using either the tabulated STIS LSF or a freely varying single gaussian LSF. It is clear that the improvement in χ^2 when going from two to three components is extremely high whichever LSF is used. This is particularly true for Fe II in which case the improvement can be seen directly on Figure 6. Indeed if one looks closely at the Fe II lines, one can see an asymmetry of the line profile of the bluer component which is common to all Fe II lines. This constitutes clear evidence for the presence of three absorbing components and not two. One sees this third component in Fe II and not in other lines since Fe II is the heaviest species, and its line widths are thus the smallest. Moreover its lines have been observed through the echelle presenting the higher resolving power (100,000). This suffices to reveal the double structure of component B: components B1 and B2 are separated by $3.8 \pm 0.5 \text{ km s}^{-1}$ (2σ), *i.e.* of the order of the E140H spectral resolution but more than that of the E230H. The radial velocities of the three components is estimated as $v_{B1} = 7.7 \pm 0.5 \text{ km s}^{-1}$, $v_{B2} = 11.5 \pm 0.5 \text{ km s}^{-1}$ and $v_{LIC} = 19.4 \pm 0.5 \text{ km s}^{-1}$, with 1σ errors due to the wavelength calibration. The LIC velocity is in perfect agreement with its projected velocity on the line of sight.

One can also see further evidence for the double structure B1-B2 in the S III 1190.2Å

line shown in the upper right panel of Fig. 7. This line is seen only in the bluest component B1, which reflects the difference in ionization between the various components; its spectral position is quite precisely known as it is located close to the Si II line at 1190.4Å and is seen in two different spectral orders (see Table 6). Note that the position of most lines is actually very well controlled, which is important to determine the number of absorbing components. In effect, the sharp geocoronal lines of N I, O I and O I* are in several locations (see Fig. 7), notably close to interstellar lines of N I, O I and Si II. Other Si II lines or Fe II lines are well constrained since in each of these species the absorption due to the LIC is sharp and pronounced, and serves as a useful spectral reference.

In order to test the hypothesis that the presence of a third component is not required by the fit, we perform an F -test. This test uses the Fisher-Snedecor law which describes the probability distribution of the χ^2 ratio. Here we test the probability that the decrease of the χ^2 due to the inclusion of a third component could be due to the increase of free parameters and not to actual information contained in the data. The result is shown species by species and for all species fitted simultaneously in Table 7, and gives a probability $\leq 10^{-4}$ that this third component is not required by the data. The F -tests performed species by species also confirm our previous impression that Si II and Fe II are the two most sensitive species to the presence of this component. We also note that the need for a third component is present whichever LSF is used.

We note that the χ^2 values corresponding to the use of the tabulated STIS LSF are too high, as they all lie above the upper 95.5% confidence level limit for statistical fluctuation (an exception being Fe II for three components). In contrast, the χ^2 values for a freely varying single gaussian LSF are satisfactory, since only O I and Si II stand out with χ^2 beyond the 95.5% confidence level for the three component solution. Their high χ^2 propagates into the total χ^2 summed over all windows. However the Si II 1190Å, 1193Å and O I 1302Å lines are saturated, and small errors in the estimates of the error bars at the bottom of the line could potentially explain large differences in χ^2 . In effect our procedure of rescaling the χ^2 amounts to rescaling all error bars by a common factor, which may not be correct for pixels at the bottom of saturated lines for the following reason. Error bars on flux values arise as a combination of background noise, fixed pattern noise and Poisson noise. Background noise dominates for pixels with flux values close to zero, while for high S/N data Poisson noise or fixed pattern noise would dominate in the continuum. If the errors in the estimation of the noise array for the background component and for the continuum component (fixed pattern or Poisson) are different, then the procedure of rescaling error bars with a common factor is, strictly speaking, incorrect. Finally, since this rescaling factor was estimated from the continuum, this rescaling should be correct for all pixels whose error is not dominated by the other noise component (background). We also note that this O I line has a complex profile,

with two geocoronal and one nearby photospheric feature (see Figure 7). Nevertheless, we decided to keep this line in our analysis as it adds important constraints on the B1 and LIC component T and ξ parameter evaluations.

Using the F -test, we can determine the probability that the use of the freely varying Gaussian LSF is not required (instead of using the STIS LSF). In all cases, it is found that this probability is smaller than 10^{-4} , and therefore we conclude that the gaussian LSF with a width that varies from spectral region to spectral region is required to fit the STIS data. This result may be unexpected but it can find a simple explanation in the fact that the tabulated STIS LSF is an average LSF given over the whole spectral range, while our gaussian LSF has a FWHM that varies with wavelength. For standard datasets it is probably sufficient to use the STIS LSF but the very high quality of the present data necessitates higher order corrections to this LSF. In particular we noted a slight broadening of the LSF near the order edges. Furthermore, the wings of the tabulated LSF are not so important and the single gaussian LSFs are sufficient to properly fit the data.

We thus conclude that three absorbers are present on the line of sight to G191-B2B.

3.2. Lyman α

The background level is directly measured at the bottom of the strongly saturated Lyman α line. It is found to be of the order of $-1.0(\pm 1.0)\%$ (2σ) of the nearby continuum, i.e. within a few percent. Variations in the photospheric continuum over the interstellar Lyman α line presents an additional difficulty. Indeed the instrument sensitivity over this spectral region is evaluated by using model spectra of white dwarfs and comparing them to the data, and one of the calibration WDs used is G191-B2B itself. Therefore it is difficult to separate the instrumental effects from the photospheric intrinsic profile in the spectrum processed through the STIS pipeline. For this reason, we follow the approach detailed in Vidal-Madjar *et al.* (1998) and further discussed by Vidal-Madjar (2000), and evaluate simultaneously all parameters and the stellar continuum, which we model in two different ways. In the first approach, we model this continuum as a polynomial whose parameters are adjusted during the fitting procedure, and which represents the real photospheric profile times the instrument sensitivity; we denote this fitting model “ U ”, which stands for uncorrected (as the data have not been corrected prior to the fit by a stellar model). In the second approach, we correct the data prior to the fit by a stellar model and keep a free low-order polynomial during the fit which models the inaccuracy of the stellar model and the variation of the instrument sensitivity; we denote this approach by “ C ”. The calculated stellar model was shifted by 24.56 km s^{-1} in order to be consistent with the velocity of the photospheric features clearly

detected in N v and Si III (see Figure 7). These two approaches have been followed in parallel to estimate the uncertainty in the modeling of the stellar continuum on the final solution.

We use two models to compute the photospheric Lyman α line profile. First, we use the program SYNSPEC (I. Hubeny 2000, private communication) in conjunction with the TLUSTY NLTE metal line-blanketed model described above. This version of SYNSPEC contains the Lemke’s Stark broadening tables for hydrogen, which were computed by Lemke (1997) within the framework of Vidal, Cooper, & Smith (1973). Second, we use Detlev Koester’s LTE code and his best fit parameters derived under the assumption of pure-H LTE ($T_{\text{eff}} = 60880$ K and $\log g = 7.59$). Figure 8 shows the NLTE and LTE Lyman α line profiles and illustrates that NLTE effects are significant only in the core of the line, which is formed high in the atmosphere where departures from LTE are important (Wesemael *et al.* 1980). However, as is shown in Fig. 8 the observations do not contain any information in that central region of the photospheric line simply because it is lost at the bottom of the saturated interstellar Lyman α line. Our fitting procedure will however be able to test the slightly different slopes in the wings of the models.

An additional correction made by a low-order polynomial is needed not only to take into account uncertainties in the instrument sensitivity but also because when one fits a section of the G191-B2B stellar continuum devoid of stellar or interstellar absorption, it is necessary to model the continuum with a polynomial of degree of order 1 to 3 for a spectral width of order 0.3\AA (see for instance Fig. 7). For a spectral region of width $\sim 3\text{\AA}$ as is the case for Lyman α , a 6th order polynomial provides a satisfactory approximation to the stellar continuum.

The best-fit solutions obtained for 3 components on the line of sight for all lines in the STIS domain including Lyman α and for various models (prior correction or not of the Lyman α stellar continuum, type of LSF) are summarized in Table 8. The zero point wavelength of the Lyman α spectral domain was found to be compatible with the other regions well within the 1σ uncertainty of 0.5km s^{-1} .

Concerning the fit with a free double gaussian (model 5 in Table 8), we found that the wings of the broader gaussian (about 5 to 10 times larger than the narrow one) contribute in amplitude (relatively to the amplitude of the narrow core gaussian) to less than 1% in all but 5 spectral windows, less than 2% in 3 of these 5 and to about 3% in the 2 remaining ones. Since this effect is marginal, we kept only as comparison tests the use of both the tabulated STIS LSF or the simple gaussian LSF. All these effects were included in the evaluation of the statistical errors.

It appears that different values of $N(\text{H I})$ are obtained depending on the model used; in

particular the comparison of models 1 and 2 on the one hand, and of models 3 and 4 on the other hand shows that the value of $N(\text{H I})$ derived depends whether the stellar continuum at Lyman α has been corrected or not beforehand by a theoretical stellar profile. One obtains $\log N(\text{H I})=18.37$ for an uncorrected profile, and $\log N(\text{H I})=18.32$ for a corrected stellar profile. Since there is no significant difference in χ^2 between these solutions, this discrepancy must be interpreted as a systematic uncertainty tied to the choice of modeling of the continuum. A $\Delta\chi^2$ analysis around each of these solutions give a statistical error of ± 0.01 dex (1σ), so that the value of $N(\text{H I})$ is dominated by the above systematic error. Furthermore after correction of the stellar continuum by an LTE calculation, which as shown in Fig. 8 represents an intermediate situation between NLTE and non-corrected stellar profiles, the value of $N(\text{H I})$ derived was found to be an intermediate value between the above two.

However a further systematic error appears if additional weak hot components are present on the line of sight, and its investigation is the subject of the following Section.

3.3. Systematic uncertainties and additional hot components

One cannot exclude the presence of weak H I components which could perturb or bias the measurement of $N(\text{H I})$, but could not be detected in any other species due to their weak column density. Such absorbers could arise as the signature of high velocity shocks (Cowie *et al.* 1979), or as cloud interfaces with the hot gas within the local ISM (Bertin *et al.* 1995) or as “hydrogen walls”, i.e., the shock interaction between the solar wind (or stellar wind) and the surrounding ISM (Linsky 1998). The latter possibility has been modeled by Wood *et al.* (2000), and a prediction for the line of sight toward G191-B2B is shown in Fig. 9 overlaid on the STIS data. It shows that most of the expected absorption should take place in the saturated core of the interstellar line, but some weak absorption ($\sim 5\%$) may be present, extending over several tenths of an Angstrom on the red side of the line, due to the neutral hydrogen atoms seen behind the shock in the downwind direction where G191-B2B is located.

We have thus investigated the possible impact of additional weak hot components on the determination of $N(\text{H I})$. In order to do so, we have added one or two additional components in H I only, and performed the fit of all lines as before with an NLTE correction of the Lyman α profile and using a free single Gaussian LSF (model 3). In order to constrain the presence of these extra absorbers, we have added to the fit the four Lyman β lines observed through the *FUSE* HIRS aperture. For each new model characterized by the number of additional components, we have measured $N(\text{H I})$ using a $\Delta\chi^2$ analysis. The best fit solutions with zero, one and two extra absorbers are shown for Lyman α and Lyman β in

Fig. 10. We have found that this introduction of additional components leads to a substantial decrease of the total $N(\text{H I})$ together with a significant improvement of χ^2 . In particular, we found that the best fit solution for one extra component leads to $\Delta\chi^2 = 26$ (1961 d.o.f.) and $\log N(\text{H I})=18.24$, and two extra components lead to $\Delta\chi^2 = 39.4$ (1958 d.o.f.) and $\log N(\text{H I})=18.11$. The χ^2 values quoted have been rescaled by a factor 1.53 corresponding to the STIS data obtained in the previous section, and which remains close (20%) to the factor measured in the *FUSE* data range. Moreover, if a $\Delta\chi^2$ analysis is performed for each model, the curve obtained flattens for low values of $N(\text{H I})$ down to $\log N(\text{H I})=18.0$; in other words, the space of solutions becomes degenerate in the low $N(\text{H I})$ region, and consequently the value of $N(\text{H I})$ measured from the profile fitting of the Lyman α region is subject to a large systematic uncertainty. This behaviour can be explained as follows. In the three component best fit solution, most of the hydrogen is contained in the LIC whose absorption makes the red wing of Lyman α . In the solutions with extra absorbers, the combined profile of these hot components can replace the damping wing contribution of the LIC, as shown in Fig. 10.

In order to scan the parameter space, the $N(\text{H I})_{\text{LIC}}$ has been forced to take various values, since the profile fitting code cannot force the total H I column density to take a particular value. When the LIC $N(\text{H I})$ becomes negligible with regards to the total $N(\text{H I})$, we force the next dominant component to take various values of $N(\text{H I})$. In this way it is possible to scan the parameter space of the total $N(\text{H I})$. One finds that once the LIC has become negligible, component B2 makes most of the total $N(\text{H I})$, and that when the total $N(\text{H I})$ is taken below 18.0, the χ^2 rapidly increases, which gives the final error bar on the total $N(\text{H I})$ estimate.

At this stage, one should point out that these best-fit solutions are quite difficult to find. The impact of additional weak absorbers on the profile fitting of $N(\text{H I})$ had already been studied by Vidal-Madjar *et al.* (1998) but no significant effect had been found, as the above solutions had eluded detection. The above solutions have actually been obtained only in a late stage of the present work. We interpret this as evidence for the fact that the χ^2 surface becomes complex when additional unconstrained absorbers are introduced in the fit of the fully blended Lyman α profile and optimization is then delicate.

One should also remark that we have modeled these extra absorbers using Voigt profiles, which implicitly assumes a Maxwellian distribution for the velocities of the atoms. However if these absorbers correspond to interstellar structures similar to hydrogen walls, the latter assumption is incorrect and the overall profile should be closer to that modeled by Wood *et al.* (2000) and shown in Fig. 9. For this reason, the above modeling and solutions should be interpreted as a first approximation. For this reason as well, we do not discard the values

for $N(\text{H I})$ obtained in the previous section without additional absorbers, even though the presence of extra absorbers induce a significant gain in χ^2 . At the worst the final value for $N(\text{H I})$ will be more conservative. With these remarks in mind, we conclude that the total hydrogen content toward G191-B2B should be contained in the interval:

$$18.00 \leq \log N(\text{H I}) \leq 18.37.$$

In the absence of any indication on the distribution of the errors for $N(\text{H I})$, we consider the above two extreme values as 2σ limits since they correspond to rather extreme solutions, and quote the following value for $N(\text{H I})$: $\log N(\text{H I}) = 18.18 \pm 0.09$ (1σ error). One should note that this effect of additional absorbers had not been found in previous studies of the total hydrogen content toward G191-B2B. Therefore it is important to remark that the above large uncertainty must also affect the previous values of $N(\text{H I})$. In other words, the above results supersedes any previous estimate of $N(\text{H I})$ made toward G191-B2B using profile fitting of the Lyman α line. One may also wonder whether extra absorbers may affect the determination of $N(\text{H I})$ toward other stars; this important question is the subject of a forthcoming paper (Vidal-Madjar & Ferlet 2002). On the other hand, the above value for $N(\text{H I})$ should be contrasted with the value derived from EUVE observations and modeling of the atmosphere of G191-B2B which gave $\log N(\text{H I}) = 18.315 \pm 0.013$ (Dupuis *et al.* 1995, 2σ error), $\log N(\text{H I}) = 18.32$ (Lanz *et al.* 1996, no error bar quoted) and the recent detailed measurement $\log N(\text{H I}) = 18.30 \pm 0.09$ (Barstow & Hubeny 1998; this value also agrees with the more recent work of Barstow, Hubeny & Holberg 1999). These values would tend to indicate that the contamination of the Lyman α profile by weak hot absorbers (if any) is not important, as they agree with the values we obtained without including such extra absorbers. However, as noted in Barstow & Hubeny (1998), these fits of the EUVE spectrum of G191-B2B typically lead to very large and unexplained reduced χ^2 , implying that the overall fit is not yet satisfactory in spite of the use of sophisticated WD atmosphere models, and that some unknown effects have yet to be accounted for.

4. Discussion and conclusions

We have measured the total column densities of D I, N I and O I toward G191-B2B using unsaturated absorption lines of these elements in high quality *FUSE* spectra. After a careful examination of the possible systematic uncertainties tied to the choice of the stellar continuum and to the instrumental configuration, we have derived the following column densities with 2σ uncertainties:

$$\begin{aligned}\log N(\text{D I})_{\text{tot}} &= 13.40 \pm 0.07, \\ \log N(\text{O I})_{\text{tot}} &= 14.86 \pm 0.07, \\ \log N(\text{N I})_{\text{tot}} &= 13.87 \pm 0.07.\end{aligned}$$

We have also analyzed new high signal-to-noise ratio high resolution STIS observations of G191-B2B and provided concrete evidence for the presence of at least three interstellar absorbing components on the line of sight by analyzing the interstellar absorption lines of N I, O I, Si II, Si III, S III and Fe II present in the STIS bandpass. We have also measured the total hydrogen column density on the line of sight using the velocity structure derived from the above metals. We have performed an exhaustive study of systematic effects on the value of $N(\text{H I})$. In particular we have discovered a new major source of uncertainty on $N(\text{H I})$ tied to the possible presence of additional weak hot absorbers whose combined absorption profile can contribute significantly to the wings of the blended Lyman α profile. The column density of these absorbers is small compared to the other main components, and they would not be detected in any other species than H I, but their contribution to the Lyman α absorption profile can reduce significantly the total H I column density measured from the profile fitting. In order to constrain their impact, we have analyzed simultaneously Lyman α and the higher order Lyman lines, and concluded that the best value of $N(\text{H I})$ toward G191-B2B is:

$$\log N(\text{H I})_{\text{tot}} = 18.18 \pm 0.18 \quad (2\sigma \text{ error})$$

We emphasize that this uncertainty is a systematic uncertainty which had gone unnoticed before. Therefore the above result supersedes previous estimates of $N(\text{H I})$ toward G191-B2B obtained from the profile fitting of Lyman α . A detailed analysis of this uncertainty and its consequences on $N(\text{H I})$ determinations toward other stars is discussed in a companion paper (Vidal-Madjar & Ferlet 2002). We thus derive the following neutral abundance ratios toward G191-B2B, with 2σ uncertainties:

$$\begin{aligned}(\text{D}/\text{H})_{\text{tot}} &= 1.66^{+0.9}_{-0.6} 10^{-5} \\ (\text{D}/\text{O})_{\text{tot}} &= 3.49 \pm 0.78 10^{-2} \\ (\text{D}/\text{N})_{\text{tot}} &= 3.41 \pm 0.76 10^{-1} \\ (\text{O}/\text{H})_{\text{tot}} &= 4.79^{+2.5}_{-1.7} 10^{-4} \\ (\text{N}/\text{H})_{\text{tot}} &= 4.90^{+2.6}_{-1.8} 10^{-5}\end{aligned}\tag{1}$$

Most of the uncertainty in the above result results from the systematic uncertainty on the $N(\text{H I})$ determination. This clearly shows the importance of measuring accurate (D/O) and (D/N) ratios in the interstellar medium instead of abundances relative to hydrogen, as emphasized by Timmes *et al.* (1997). Interestingly if one uses the recent measurement of $N(\text{H I})$ from the modeling of the atmosphere of G191-B2B and the fit of the EUVE spectrum, $\log N(\text{H I}) = 18.30 \pm 0.09$ (2σ), one finds $(\text{D}/\text{H})_{\text{tot}} = 1.26_{-0.29}^{+0.36} \times 10^{-5}$ (2σ). At this stage, however, due to the uncertainty inherent to the modeling of the white dwarf atmosphere, it is probably more conservative to use the interstellar determination for $N(\text{H I})$, and therefore the previous value of the (D/H) ratio.

The above new value for the (D/H) ratio agree with the range of values measured by Linsky (1998) toward a dozen stars of the LISM and with the values previously derived toward G191-B2B. However the discrepancy between previous estimates of the (D/H) ratio toward G191-B2B and the LISM average D/H ratio has disappeared due to a revision of the uncertainty on the estimation of the total H I content. A detailed interpretation of this (D/H) value and of the accompanying (D/O) and (D/N) ratios and their implications is provided in a companion paper by Moos *et al.* (2002).

Financial support to U.S. participants has been provided by NASA contract NAS5-32985. French participants are supported by CNES.

REFERENCES

- Allen, M.M., Jenkins, E.E., & Snow, T.P., 1992, ApJS, 83, 261
- Audouze, J., Tinsley, B. M., 1976, ARA&A, 14, 43
- Barstow, M.A., Hubeny, I., & Holberg, J. B., 1998, MNRAS, 299, 520
- Barstow, M. A., Holberg, J. B., & Koester, D., 1995, MNRAS, 274, L31
- Barstow, M. A., Hubeny, I., 1998, MNRAS, 299, 379
- Barstow, M. A., Hubeny, I., Holberg, J. B., 1999, MNRAS 307, 884
- Barstow, M. A., *et al.* 2001, in *The 12th European Workshop on White Dwarfs*, ASP Conf. Series, in press
- Bertin, P., *et al.*, 1995, A&A, 302, 889
- Boesgaard, A. M., Steigman, G., 1985, ARA&A, 23, 319

- Burles, S., 2001, in *Gaseous matter in galaxies and intergalactic space - XVIIth IAP Colloquium* (Paris, June 19-23 2001), eds. R. Ferlet *et al.* (Frontier Group), in press.
- Cassé, M., & Vangioni-Flam, E., 1998, in *Structure and Evolution of the Intergalactic Medium from QSO Absorption Line Systems*, eds. P. Petitjean and S. Charlot (IAP Conference series), 331
- Cowie, L., *et al.*, 1979, ApJ, 229, L81
- Dupuis, J., *et al.*, 1995, ApJ, 455, 574
- Dupuis, J., *et al.*, 1998, ApJ, 500, L45
- Ferlet, R., *et al.*, 1980, ApJ, 242, 576
- Friedman, S.D., *et al.*, 2002, ApJ, submitted
- Gautier, D., Owen, T., 1983, Nature, 302, 215
- Geiss, J., Reeves, H., 1972, A&A, 18, 126
- Gry, C., Lamers, H. J. G. L. M., Vidal-Madjar, A., 1984, A&A, 137, 29
- Hébrard, G., Mallouris, C., Ferlet, R., Koester, D., Lemoine, M., Vidal-Madjar, A., & York, D. G., 1999, A&A, 350, 643
- Hébrard, G., *et al.*, 2002, ApJ, submitted
- Howk, J. C., Sembach, K. R., 2000, AJ, 119, 2481
- Hubeny, I., Lanz, T., 1995, ApJ, 439, 875
- Jenkins, E. B., Tripp, T. M., Woźniak, P. R., Sofia, U. J., Sonneborn, G., 1999, ApJ, 520, 182
- Kruk, J. W., *et al.*, 2002, ApJ, submitted
- Landsman, W., Sofia, U. J., Bergeron, P., 1996, in *Science with the Hubble Space Telescope - II*, STScI, 454
- Lanz, T., Barstow, M. A., Hubeny, I., Holberg, J.B., 1996, ApJ, 473, 1089
- Laurent, C., Vidal-Madjar, A., York, D.G., 1979, ApJ, 229, 923
- Lehner, N., *et al.*, 2002, ApJ, submitted

- Lemke, M., 1997, A&AS, 122, 285
- Lemoine, M., Vidal-Madjar, A., Bertin, P., Ferlet, R., Gry, C., & Lallement, R., 1996, A&A, 308, 601
- Lemoine, M., *et al.*, 1999, New Astronomy, 4, 231
- Linsky, J. L., 1998, Space Science Reviews, 84, 285
- Moos, H.W., *et al.*, 2000, ApJ, 538, L1
- Moos, H.W., *et al.*, 2002, ApJ, submitted
- Pagel, B., *et al.*, 1992, MNRAS, 255, 325
- Prantzos, N., 1996, A&A, 310, 106
- Rogerson, J., York, D. G., 1973, ApJ, 186, L95
- Sahnow, D.J., *et al.*, 2000, ApJ, 538, L7
- Sahu, M. S., Landsman, W., Bruhweiler, F. C., Gull, T. R., Bowers, C. A., Lindler, D., Feggans, K., Barstow, M. A., Hubeny, I., Holberg, J. B., 1999, ApJ, 523, L159
- Sahu, M. S., 2000, in *The Light Elements and Their Evolution*, eds. L. da Silva, M. Spite, J. R. de Medeiros (ASP Conference Series), 161
- Scully, S. T., *et al.*, 1997, ApJ, 476, 521
- Sonneborn, G., Tripp, T. M., Ferlet, R., Jenkins, E. B., Sofia, U. J., Vidal-Madjar, A., Woźniak, P. R., 2000, ApJ, 545, 277
- Sonneborn, G., *et al.*, 2002, ApJ, submitted
- Timmes, F. X., Truran, J. W., Lauroesch, J. T., York, D. G., 1997, ApJ, 476, 464
- Tosi, M., Steigman, G., Matteucci, F., Chiappini, C., 1998, ApJ 498, 226
- Vangioni-Flam, E., & Cassé, M., 1994, ApJ, 427, 618
- Vangioni-Flam, E., Olive, K., & Prantzos, N., 1995, ApJ, 441, 471
- Vennes, S., Polomski, E. F., Lanz, T., Thorstensen, J. R., Chayer, P., Gull, T. R., 2000, ApJ, 544, 423
- Vennes, S., Chayer, P., Hurwitz, M., Bowyer, S., 1996, ApJ, 468, 898

- Vidal, C. R., Cooper, J., Smith, E. W., 1973, ApJS, 25, 37
- Vidal–Madjar, A., Gry, C., 1984, A&A, 138, 285
- Vidal–Madjar, A., *et al.*, 1977, ApJ, 211, 91
- Vidal–Madjar, A., Lemoine, M., Ferlet, R., Hébrard, G., Koester, D., Audouze, J., Cassé, M., Vangioni-Flam, E., Webb, J. K., 1998, A&A, 338, 694
- Vidal–Madjar, A., 2000, in *The Light Elements and Their Evolution*, eds. L. da Silva, M. Spite, & J. R. de Medeiros (ASP Conference Series), 151
- Vidal–Madjar, A., 2001, in *Cosmic Evolution*, eds. E. Vangioni-Flam, R. Ferlet, M. Lemoine (World Scientific), p.49
- Vidal–Madjar, A., Ferlet, R., 2002, in preparation
- York, D. G., 1983, ApJ, 264, 172
- York, D.G., Rogerson, J., 1976, ApJ, 203, 378
- Wesemael, F., Auer, L. H., Van Horn, H. M., Savedoff, M. P., 1980, ApJS, 43, 159
- Wood, B. E., Muller, H–R., Zank, G. P., 2000, ApJ, 542, 493
- Wood, B. E., *et al.*, 2002, ApJ, submitted

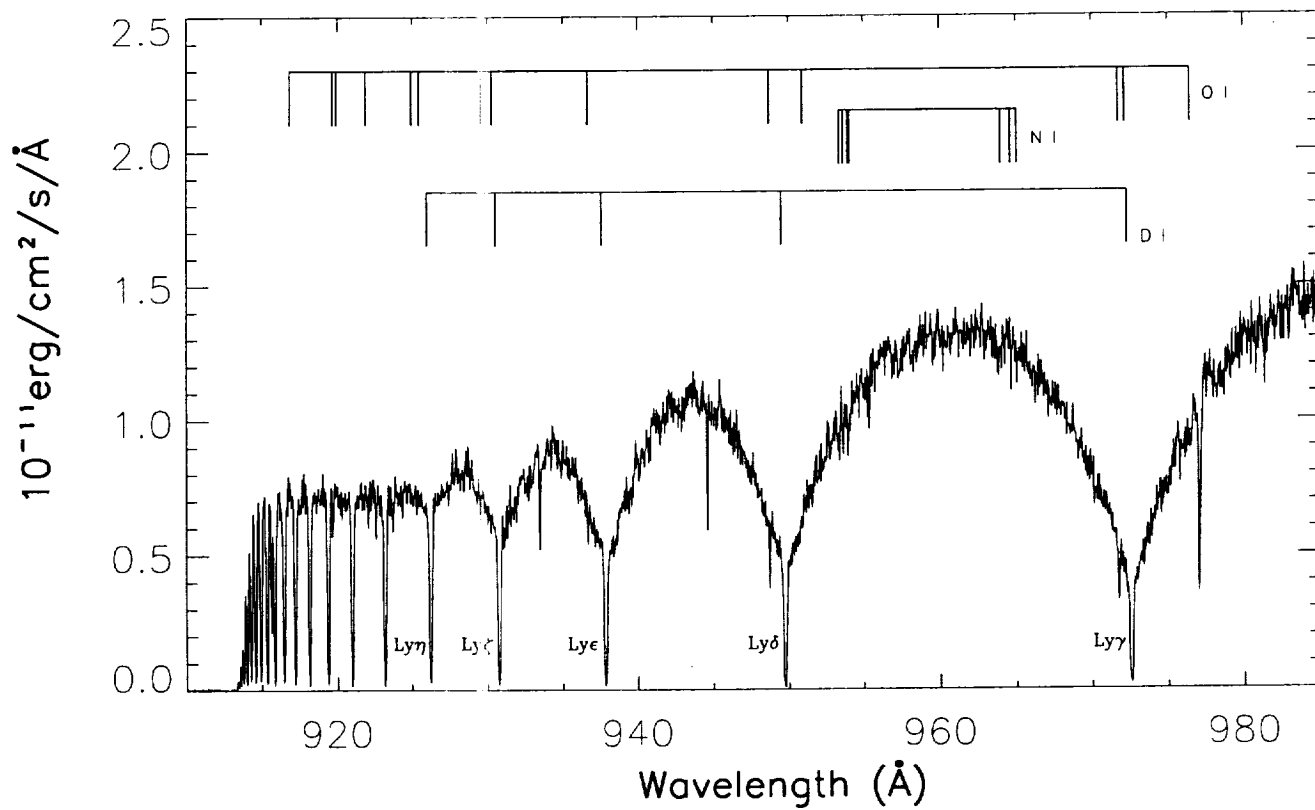


Fig. 1.— *FUSE* HIRS spectrum of G191-B2B (segment SiC1B). The Lyman series is clearly seen down to the Lyman limit. The positions of the D I, O I and N I lines considered in our study are indicated.

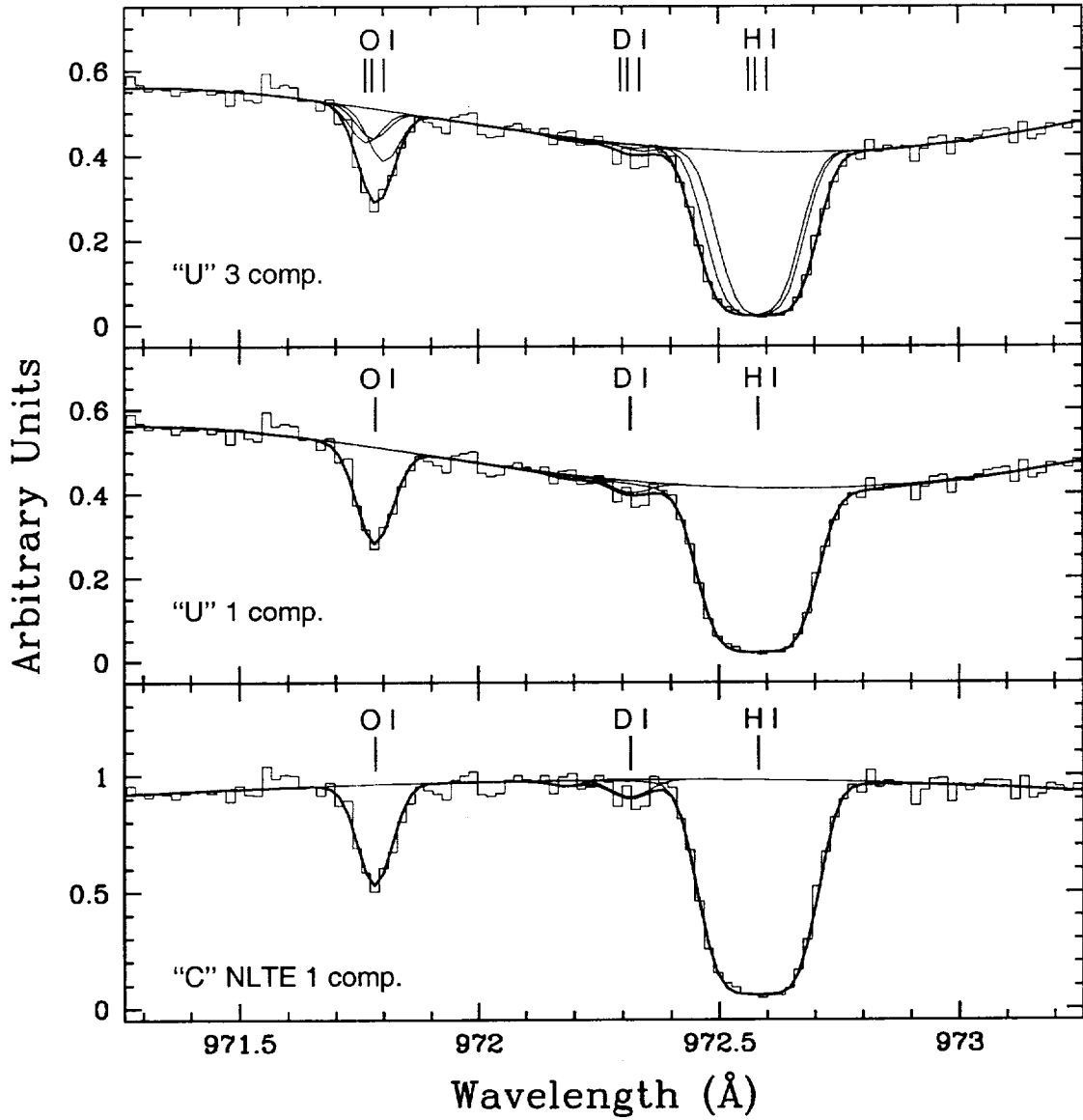


Fig. 2.— *FUSE* MDRS spectrum of G191-B2B around Lyman γ (segment SiC2A). The solid line in each panel shows the best fit obtained by a simultaneous profile fitting of all H I, D I, O I and N I lines of all *FUSE* datasets. Clearly these observations do not resolve the multiple absorbers along the line of sight. In the upper panel the continuum is interpolated by a smooth polynomial, and three interstellar components corresponding to the velocity structure of the line of sight derived from the higher resolution STIS observations (see Section 3) were considered; in the middle panel, the stellar continuum is also interpolated by a polynomial, while only one absorbing component is considered. In the lower panel the stellar continuum has been corrected by a theoretical NLTE stellar profile, the residual continuum is modeled by a polynomial and only one absorbing component has been assumed. See text for details.

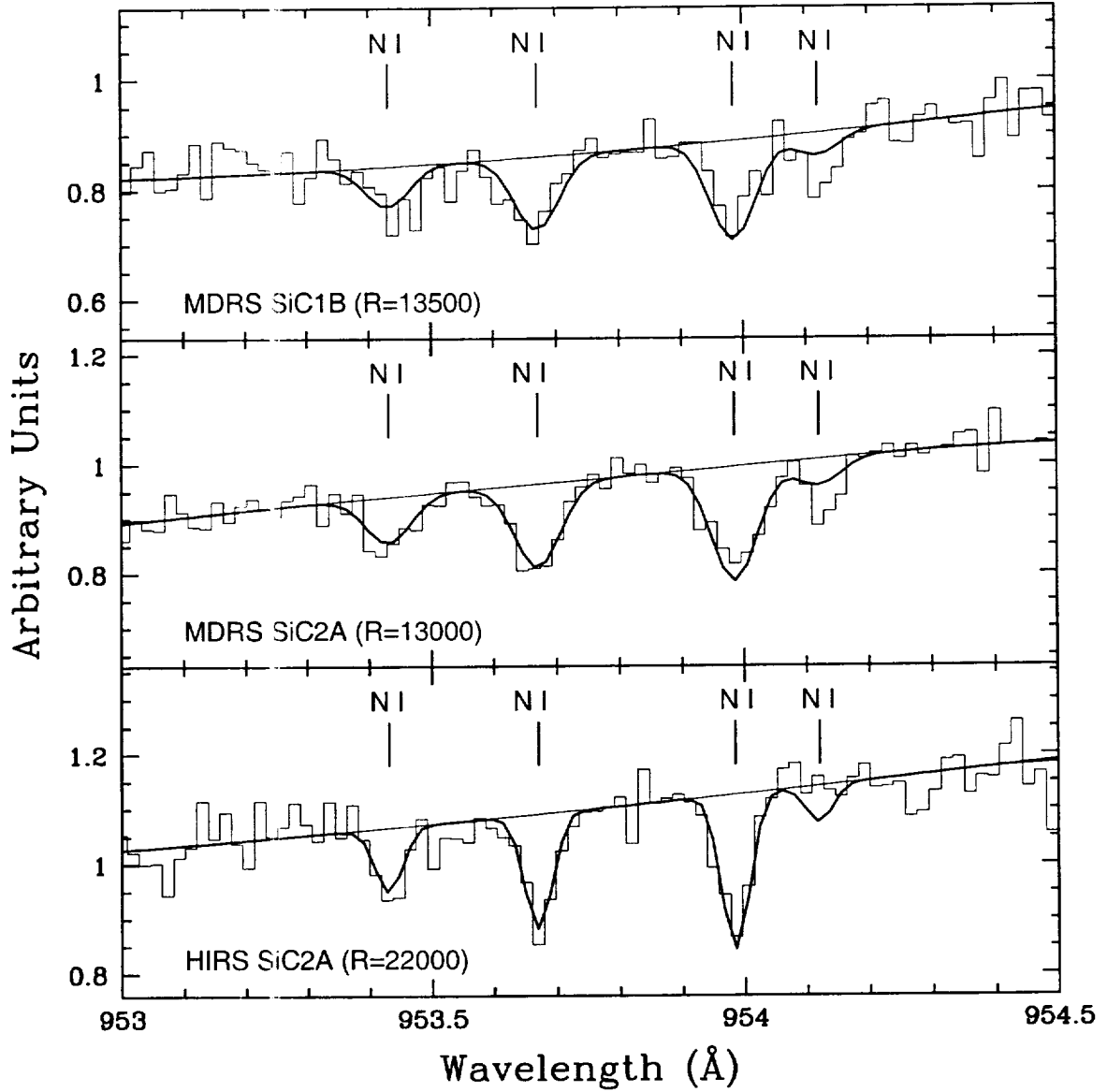


Fig. 3.— *FUSE* spectra of G191-B2B around the N I multiplet at 954Å. The aperture, segment and resolving power R corresponding to each dataset are indicated on the figure. The line at 954.1Å was excluded from the profile fitting since it is likely contaminated by a photospheric feature, as indicated by theoretical modeling of the stellar continuum, and as shown clearly in the upper and middle panels; in the lower panel, the apparent absence of this line may result from a statistical fluctuation or from a detector feature. The higher resolution of the HIRS aperture data is apparent.

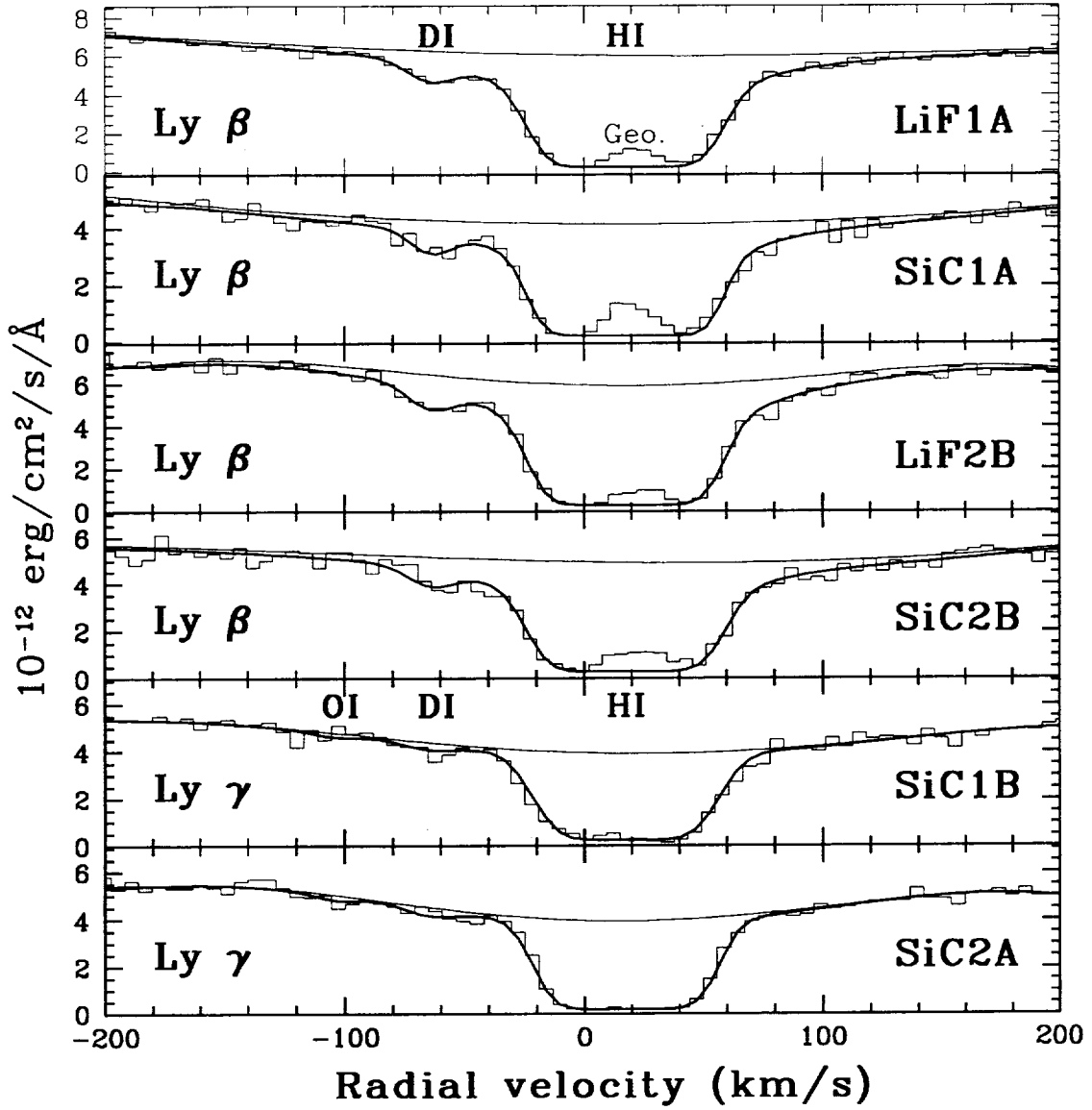


Fig. 4.— *FUSE* HIRS spectra of Lyman β and Lyman γ , recorded on the segments indicated in the figure. The solid line shows the final best-fit solution to all lines of H I, D I, N I and O I in all HIRS data fitted simultaneously. The weak emission line at the bottom of the Lyman lines is due to H I geocoronal emission; the pixels affected by this emission are not considered in the fit. The stellar continuum is interpolated by a smooth polynomial. See text for details.

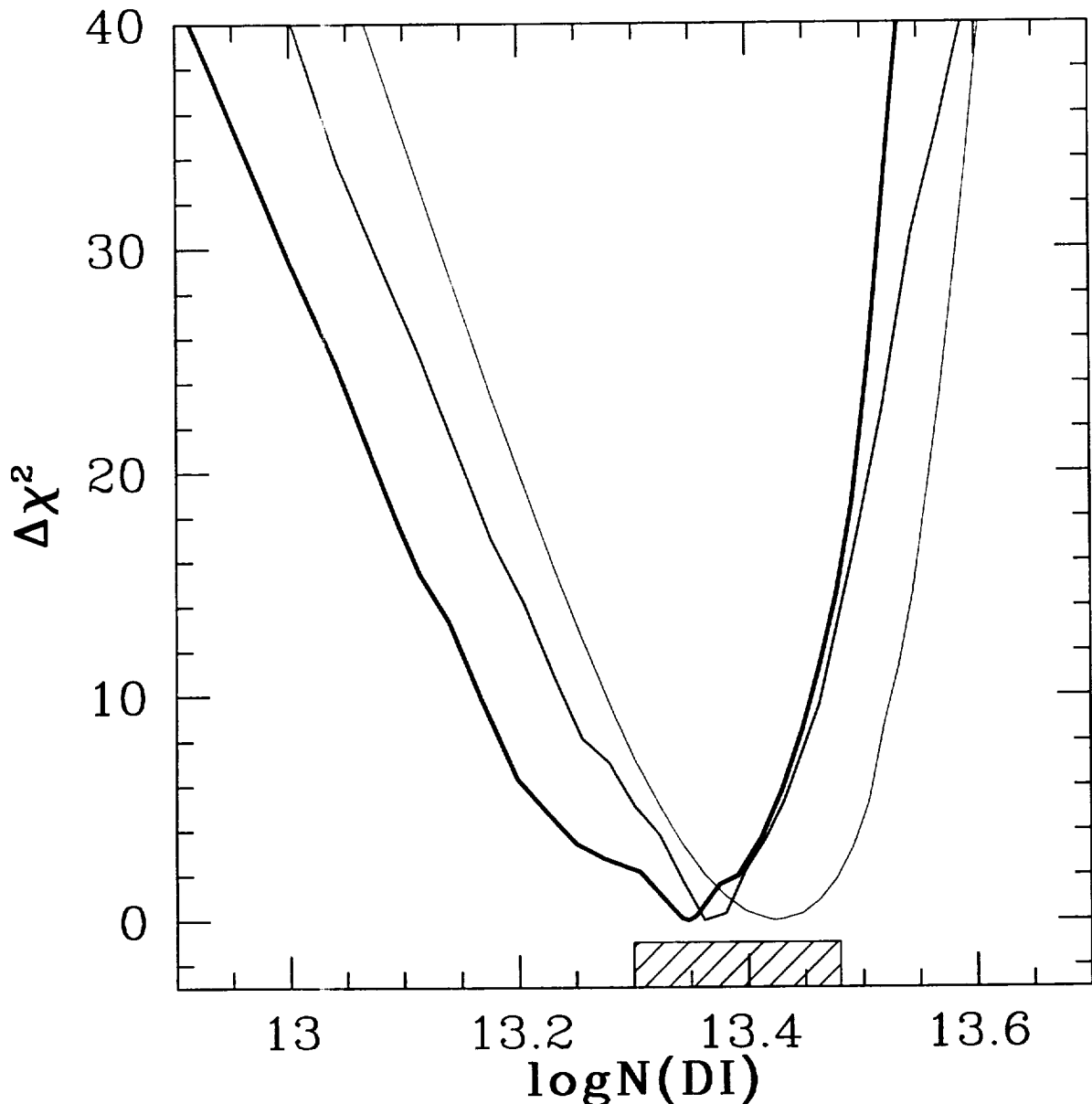


Fig. 5.— Curve of $\Delta\chi^2$ deviations around the best fit χ^2 as a function of $\log N(\text{D I})$. Only the curve for the HIRS data is shown here; statistical error bars for other aperture data were obtained using the same method. The $\Delta\chi^2$ values shown here have been rescaled to compensate for uncertainties in the individual pixel errors (see text). The various curves correspond to different models for the fit: in thick line, the D I and H I are fitted simultaneously with a LSF modeled as a single gaussian with free FWHM; in intermediate thickness, the same approach but with a double gaussian LSF, with free amplitude ratio and FWHMs; in thin line, H I is excluded from the fit, the continuum to the D I absorption is modeled by a polynomial, and the LSF is a simple gaussian. The curvature of these curves give the the statistical errors while their relative shifts give an estimate of the overall systematic uncertainty related to the different models. The hatched area shows the final 95.5% confidence level error for $\log N(\text{D I})$ measured using the HIRS data.

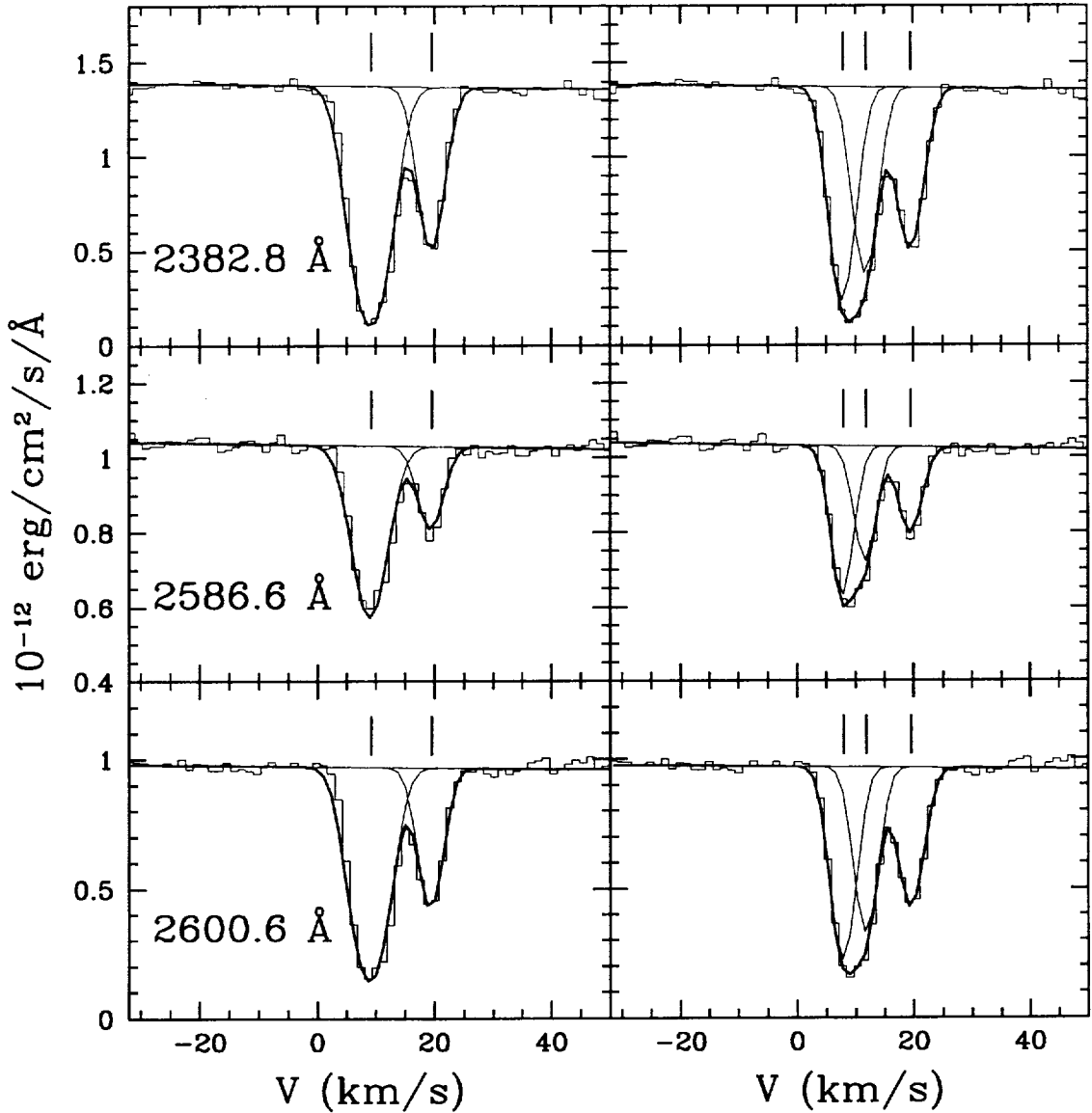


Fig. 6.— The STIS data covering the three Fe II lines observed with the E230H Echelle grating. All fits shown here were made using a freely varying single gaussian LSF; the Fe II lines were fitted simultaneously with all other species including Lyman α (see text). The left panels show the fits with two absorbing components only, and the right panels show the fits using three components. One can clearly see the same asymmetry of the bluer component *B* in all Fe II lines which reveals the presence of complex substructure in this component, hence the need for 3 absorbers in total. The χ^2 corresponding to these fits is 227.9/139 for the two component solution, and 123.3/136 for the three component solution; the gain is clear and comforts the visual impression. The error bars on each pixel are of order of 2% of the continuum level.

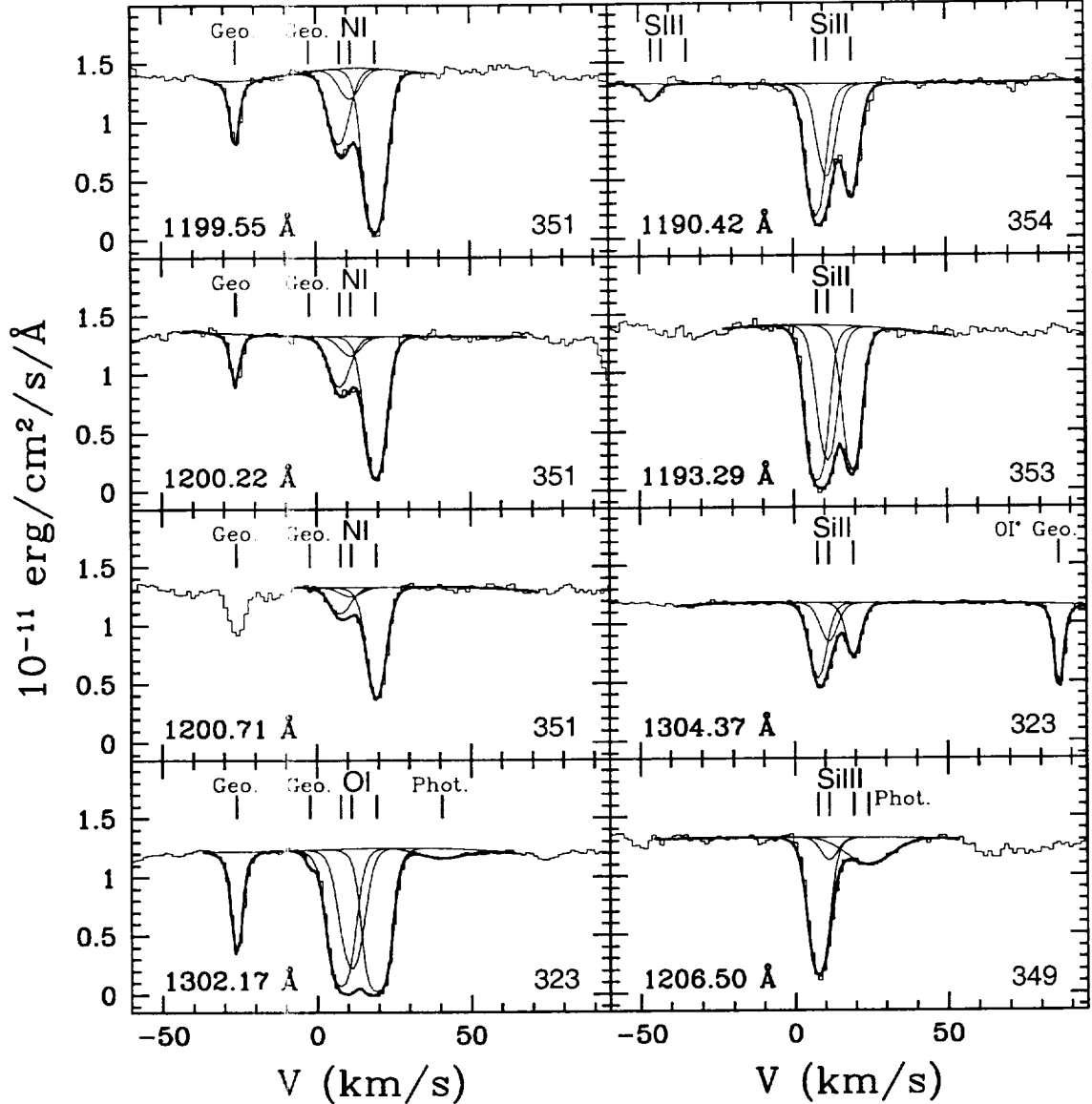


Fig. 7.— The STIS data with the best-fit three component solution using the tabulated STIS LSF; only 8 sub-spectra out of 19 in total are shown here, and are labeled with the central spectral line wavelength and Echelle order: the N I 1200Å triplet along with the nearby geocoronal absorptions (marked “Geo.”, in two different locations because two data sets taken at two different epochs are here averaged), the O I line with the corresponding geocoronal O I absorptions and a nearby photospheric feature (noted “Phot.”), three of the Si II lines with either the nearby S III feature or the O I* geocoronal absorption and the Si III line with an additional broad Si III photospheric line located at the same velocity shift as the N V photospheric line (which was fitted simultaneously). Note also that the S III lines clearly detected in two different orders near 1190.2Å are also spectrally well located. The fact that they show up only in the bluest component B1 is an additional reason why 3 and not 2 components are needed along that line of sight.

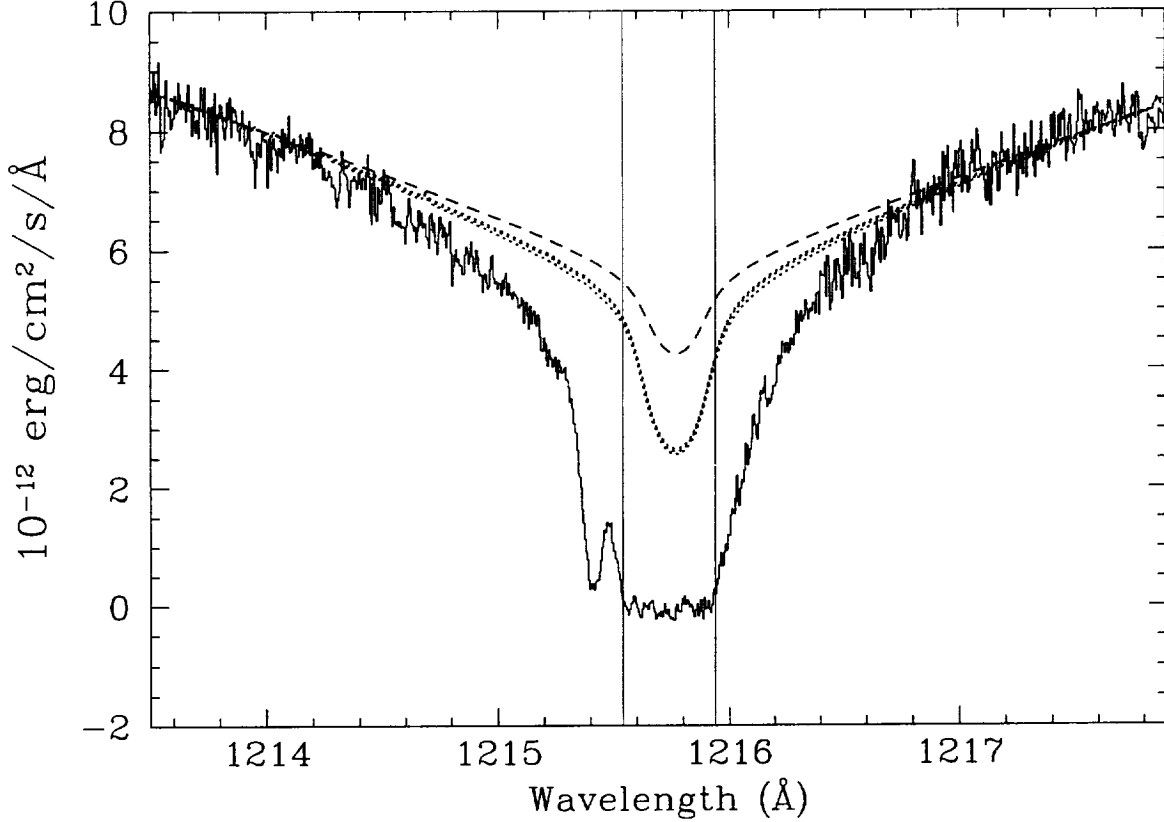


Fig. 8.— The STIS data over the Lyman α spectral region along with the LTE (dashed line) and NLTE (dotted lines) photospheric profiles. Three different NLTE profiles for atmospheric parameters in the ranges $54000 \text{ K} \leq T_{\text{eff}} \leq 55000 \text{ K}$ and $7.5 \leq \log g \leq 7.6$ are shown. The LTE calculation uses $T_{\text{eff}} = 60880 \text{ K}$ and $\log g = 7.59$. The radial velocity for the photospheric profiles is set to $+24.56 \text{ km s}^{-1}$. The two thin vertical lines delimit the wavelength range in which no information on the stellar profile is contained in the data. The fitting procedure thus tests only the difference between the wings of the models and not their cores whose difference is more pronounced.

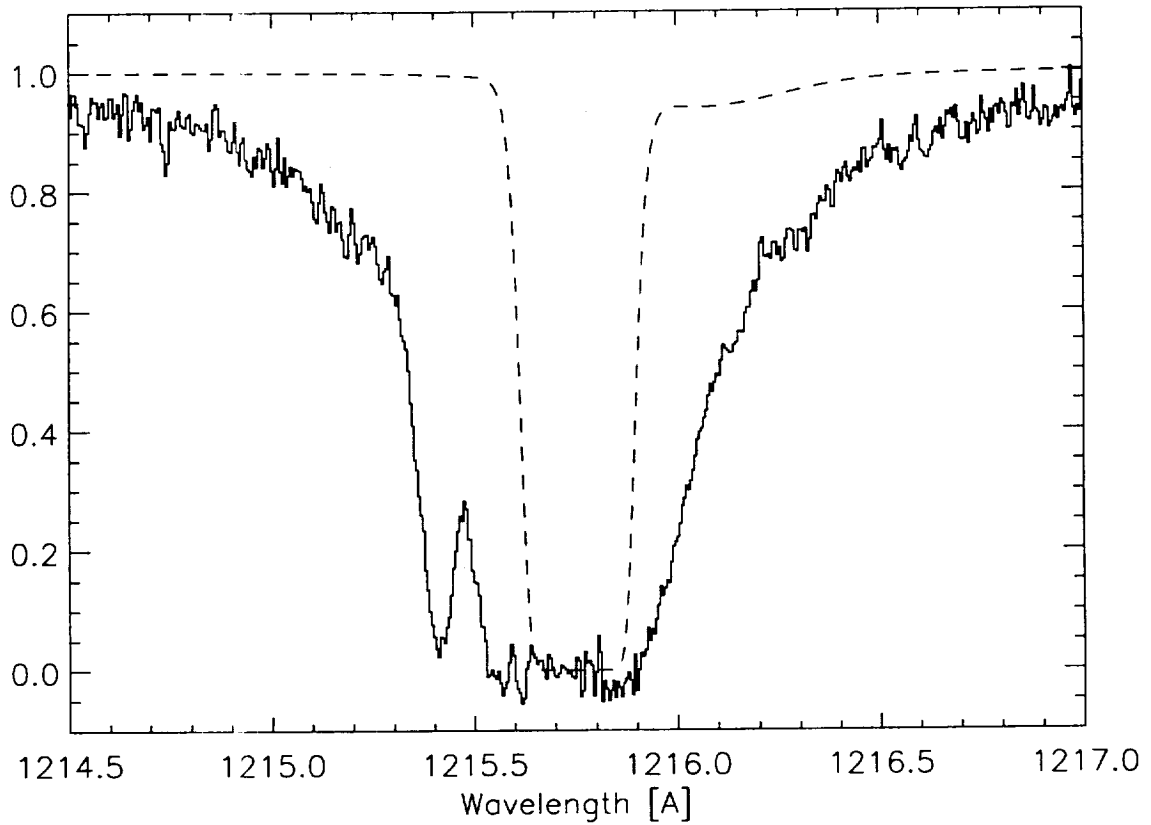


Fig. 9.— The Lyman α interstellar absorption observed with STIS with the hydrogen wall model of Wood *et al.* (2000) for the line of sight of G191-B2B overplotted in dashed line. The STIS data has been normalized by the best-fit continuum.

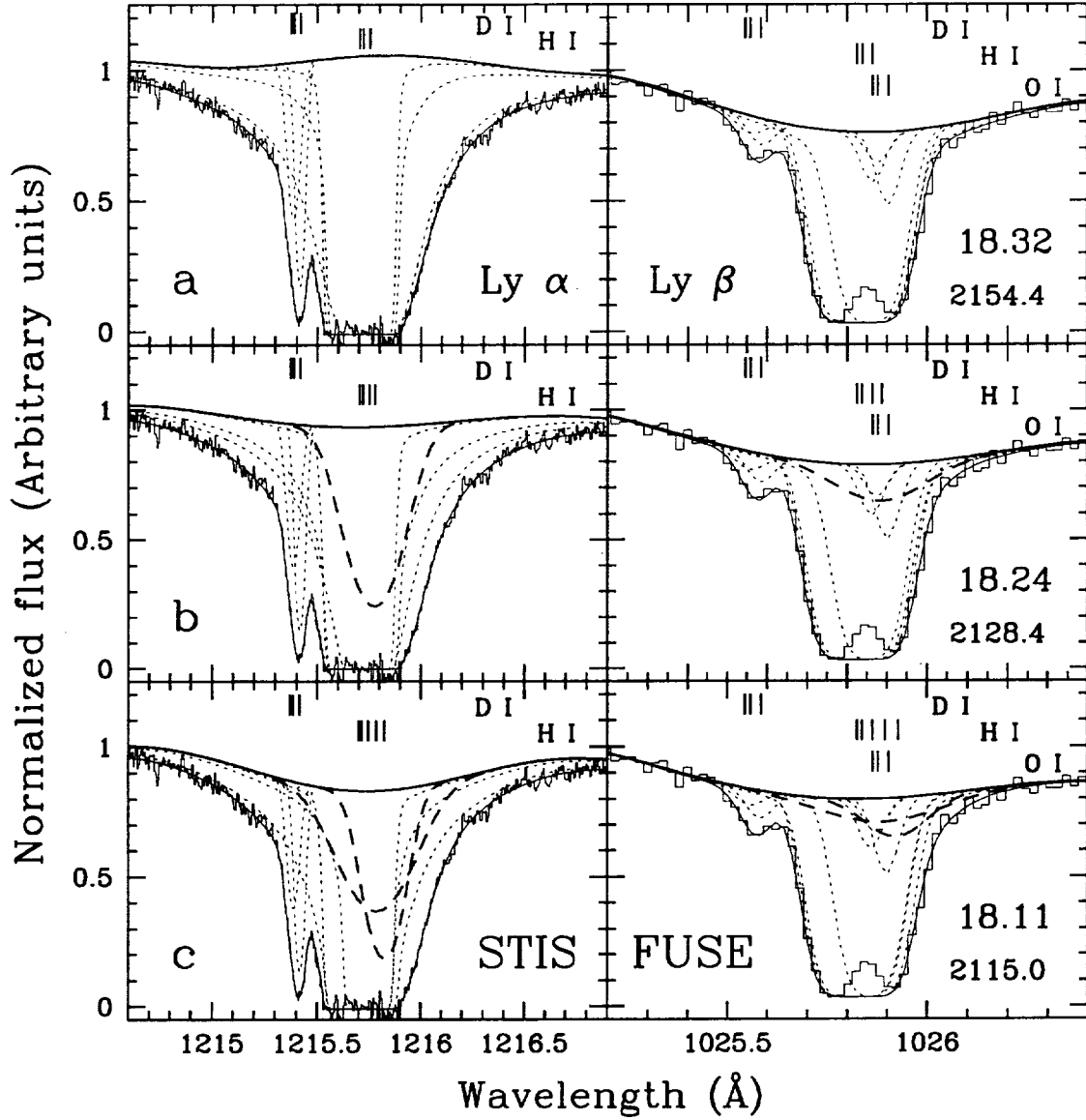


Fig. 10.— Best-fit solutions for all lines in the STIS data plus four Lyman β from the *FUSE* HIRS dataset using three main interstellar components plus zero, one and two extra H I components (upper, middle, and lower panels respectively). The total absorption profile is shown as the solid line, and the dotted and dashed lines show the individual profiles (convolved with the LSF); the thick dashed lines in particular show the contribution of the extra absorbers. The solutions are labeled with the total rescaled χ^2 (for 1964, 1961, and 1958 d.o.f. respectively for the upper, middle and lower panels) and total H I column density (in log).

Table 1. Strongest N I and O I spectral lines in the *FUSE* domain.

Wavelength (Å)	Element	f	A (s ⁻¹)	Comment
1025.4440	D I	$0.264 \cdot 10^{-1}$	$0.190 \cdot 10^9$	
1025.4429	D I	$0.527 \cdot 10^{-1}$	$0.190 \cdot 10^9$	
972.2725	D I	$0.967 \cdot 10^{-2}$	$0.813 \cdot 10^8$	
972.2721	D I	$0.193 \cdot 10^{-1}$	$0.813 \cdot 10^8$	
949.4848	D I	$0.465 \cdot 10^{-2}$	$0.421 \cdot 10^8$	Weak
949.4846	D I	$0.929 \cdot 10^{-2}$	$0.421 \cdot 10^8$	Weak
1134.9803	N I	$0.435 \cdot 10^{-1}$	$0.150 \cdot 10^9$	
1134.4149	N I	$0.297 \cdot 10^{-1}$	$0.154 \cdot 10^9$	
1134.1653	N I	$0.152 \cdot 10^{-1}$	$0.158 \cdot 10^9$	
954.1042	N I	$0.676 \cdot 10^{-2}$	$0.330 \cdot 10^8$	Blend
953.9699	N I	$0.348 \cdot 10^{-1}$	$0.170 \cdot 10^9$	
953.6549	N I	$0.250 \cdot 10^{-1}$	$0.183 \cdot 10^9$	
953.4152	N I	$0.132 \cdot 10^{-1}$	$0.193 \cdot 10^9$	
1039.2303	O I	$0.920 \cdot 10^{-2}$	$0.947 \cdot 10^8$	
1026.4757	O I	$0.246 \cdot 10^{-2}$	$0.111 \cdot 10^8$	Weak
1026.4744	O I	$0.187 \cdot 10^{-3}$	$0.118 \cdot 10^7$	Weak
1025.7633	O I	$0.201 \cdot 10^{-3}$	$0.212 \cdot 10^7$	Blend
1025.7626	O I	$0.302 \cdot 10^{-2}$	$0.191 \cdot 10^8$	Blend
1025.7616	O I	$0.169 \cdot 10^{-1}$	$0.765 \cdot 10^8$	Blend
988.7734	O I	$0.465 \cdot 10^{-1}$	$0.226 \cdot 10^9$	Strong
988.6549	O I	$0.830 \cdot 10^{-2}$	$0.566 \cdot 10^8$	Blend
988.5778	O I	$0.553 \cdot 10^{-3}$	$0.629 \cdot 10^7$	Weak
976.4481	O I	$0.331 \cdot 10^{-2}$	$0.386 \cdot 10^8$	
971.7382	O I	$0.116 \cdot 10^{-1}$	$0.585 \cdot 10^8$	Strong
971.7376	O I	$0.207 \cdot 10^{-2}$	$0.146 \cdot 10^8$	Blend
950.8846	O I	$0.158 \cdot 10^{-2}$	$0.194 \cdot 10^8$	
948.6855	O I	$0.631 \cdot 10^{-2}$	$0.100 \cdot 10^9$	
936.6295	O I	$0.365 \cdot 10^{-2}$	$0.100 \cdot 10^9$	
929.5168	O I	$0.229 \cdot 10^{-2}$	$0.100 \cdot 10^9$	
925.4460	O I	$0.354 \cdot 10^{-3}$	$0.459 \cdot 10^7$	Weak
924.9500	O I	$0.154 \cdot 10^{-2}$	$0.100 \cdot 10^9$	

Table 1—Continued

Wavelength (Å)	Element	f	A (s ⁻¹)	Comment
921.8570	O I	0.100 10 ⁻²	0.562 10 ⁷	Weak

Table 2. *FUSE* observation log of G191-B2B.

Dataset	Aperture	T_{exp} (ksec)	N_{exp}	Date
S3070101	LWRS	15.5	32	2000.01.14
P1041202	MDRS	15.5	21	2000.01.13
P1041201	HIRS	15.5	32	2000.11.06

Table 3. Published and *FUSE* O I and N I column densities.

Spectrograph / Aperture	$\log N(\text{O I})_{\text{tot}}$ 2σ error	$\log N(\text{N I})_{\text{tot}}$ 2σ error	Reference
HST GHRS-Ech.	14.84±0.04	13.90±0.02	Vidal-Madjar <i>et al.</i> 1998 ^a
<i>FUSE</i> LWRS+MDRS	14.79±0.04	13.82±0.07	This work ^b
<i>FUSE</i> MDRS	14.84±0.08	13.89±0.06	This work ^b
<i>FUSE</i> HIRS	14.88±0.06	13.84±0.07	This work ^b
<i>FUSE</i> -All	14.86±0.07	13.87±0.07	This work ^b

^aThree components were considered in the fit

^bOne interstellar component was considered in the fit

Table 4. Published and *FUSE* D I column densities.

Spectrograph / Spect./Aper.	$\log N(\text{D I})_{\text{tot}}$ 2σ error	Reference /Model
HST GHRS-Ech.	13.43 ± 0.02	Vidal-Madjar <i>et al.</i> 1998 ^a
HST STIS-Ech. #1	$13.55^{+0.07}_{-0.08}$	Sahu <i>et al.</i> 1999 ^b
HST GHRS-Ech.	13.40 ± 0.04	Sahu <i>et al.</i> 1999 ^b
<i>FUSE</i> LWRS+MDRS	$13.41^{+0.12}_{-0.07}$	D I, no H I, this work ^c
<i>FUSE</i> MDRS	13.41 ± 0.09	D I & H I, this work ^d
<i>FUSE</i> HIRS	13.36 ± 0.08	D I & H I (Fig. 4), this work ^d
<i>FUSE</i> HIRS	13.38 ± 0.06	D I & H I, double LSF, this work ^e
<i>FUSE</i> HIRS	13.42 ± 0.08	D I, no H I, this work ^c
<i>FUSE</i> All	13.40 ± 0.07	this work ^f

^a3 free absorbing components assumed in the profile fitting, and stellar continuum modeled with a low order polynomial free to vary during the fit

^b2 free absorbing components in the profile fitting, and stellar continuum fixed and modeled by NLTE calculations

^c1 free absorbing component, stellar continuum modeled by a freely varying low order polynomial, and D I fitted alone without the H I line

^d1 free absorbing component, stellar continuum modeled by a freely varying low order polynomial, and D I fitted simultaneously with the H I line

^e1 free absorbing component, stellar continuum modeled by a freely varying low order polynomial, and D I fitted simultaneously with the H I line, LSF profile modeled with a double Gaussian

^fcombination of *FUSE* models c, d and e

Table 5. Published H I column densities.

$\log N(\text{H I})_{\text{tot}} (2\sigma)$	Spectrograph	# Comp.	Continuum	Reference
18.315 \pm 0.013	EUVE	—	—	Dupuis <i>et al.</i> 1995
18.32 –	EUVE	—	—	Lanz <i>et al.</i> 1996
18.36 \pm 0.04	GHRG-G160M	3	free	Lemoine <i>et al.</i> 1996
18.38 \pm 0.02	GHRG-Ech.	3	free	Vidal-Madjar <i>et al.</i> 1998
18.30 \pm 0.09	EUVE	—	—	Barstow & Hubeny 1998
18.31 \pm 0.03	STIS-Ech. #1	2	fixed	Sahu <i>et al.</i> 1999
18.34 \pm 0.02	GHRG-Ech.	2	fixed	Sahu <i>et al.</i> 1999

Table 6. Spectral lines in the STIS domain used for the line of sight structure study.

Wavelength (Å)	Species	f	A (s ⁻¹)	Ech. Order
1334.5320	C II	0.128	0.288 10 ⁹	316
1200.7098	N I	0.0430	0.398 10 ⁹	350, 351
1200.2233	N I	0.0862	0.399 10 ⁹	350, 351
1199.5496	N I	0.130	0.401 10 ⁹	351
1242.8040	N V	0.500	0.336 10 ⁹	339
1302.1685	O I	0.0519	0.340 10 ⁹	323
1304.3702	Si II	0.0917	0.107 10 ¹⁰	323
1193.2897	Si II	0.585	0.409 10 ¹⁰	352, 353
1190.4158	Si II	0.293	0.410 10 ¹⁰	353, 354
1206.5000	Si III	1.67	0.255 10 ¹⁰	349
1259.5190	S II	0.0166	0.465 10 ⁸	334
1190.2030	S III	0.0231	0.651 10 ⁸	353, 354
2382.7651	Fe II	0.320	0.313 10 ⁹	324
2586.6499	Fe II	0.0691	0.272 10 ⁹	298, 299
2600.1729	Fe II	0.239	0.270 10 ⁹	297

Table 7. χ^2 comparison for the two and three component solutions using either the tabulated STIS LSF or freely varying single gaussian LSF.

Species	χ^2 / d.o.f. ^a 2 comp. STIS LSF	χ^2 / d.o.f. ^a 3 comp. STIS LSF	F -test prob. ^b 2 <i>vs</i> 3 comp.	χ^2 / d.o.f. ^a 2 comp. free Gaussian	χ^2 / d.o.f. ^a 3 comp. free Gaussian	F -test prob. ^a 2 <i>vs</i> 3 comp.
N I	395.0/314	382.3/311	1.7%	323.2/309	309.1/306	0.3%
O I	214.3/61	193.1/58	11%	113.9/60	101.4/57	8.3%
Si II	772.0/468	651.4/465	< 0.01%	678.6/463	553.6/460	< 0.01%
Si III ^c	210.6/152	192.8/149	0.4%	185.2/150	170.8/147	0.75%
Fe II	277.6/142	141.8/139	< 0.01%	227.9/139	123.3/136	< 0.01%
All ^d	2677.8/1270	1908.8/1259	< 0.01%	2076.7/1250	1442.5/1239	< 0.01%

^athe χ^2 has been rescaled to compensate for the inaccuracy of the noise array (see text)

^bThe F -test gives the probability that a third absorbing component is not required by the model

^cFitted simultaneously with the N V line to control the photospheric Si III line

^dIncludes C II, S II and S III

Table 8. Three component best-fit solutions for all lines in the STIS region including Lyman α .

Fit model	v_{B1} (km s ⁻¹)	v_{B2} (km s ⁻¹)	v_{LIC} (km s ⁻¹)	$\log N(\text{H I})_{\text{tot}}$	χ^2 1753 d.o.f.
1 ^{a,c}	7.7	11.2	19.4	18.32	2469.9
2 ^{b,c}	7.7	11.3	19.4	18.37	2470.1
3 ^{a,d}	7.7	11.7	19.4	18.32	2006.8
4 ^{b,d}	7.7	11.6	19.4	18.37	2001.8
5 ^{a,e}	7.7	11.6	19.4	18.33	1987.3

^adata normalized beforehand by NLTE stellar continuum, and stellar continuum residuals modeled during the fit by a 6th order polynomial

^bunnormalized data, with stellar continuum modeled during the fit by a 6th order polynomial

^cLSF corresponds to the tabulated STIS LSF

^dLSF profile modeled with a single Gaussian (free to vary during the fit)

^eLSF profile modeled with a double Gaussian (free to vary during the fit)